Atmos. Chem. Phys., 24, 12963–12983, 2024
https://doi.org/10.5194/acp-24-12963-2024

Atmospheric Chemistry and Physics
Open Access

Analysis of the day-to-day variability of ozone vertical profiles in the lower troposphere during the 2022 Paris ACROSS campaign

Gérard Ancellet[1], Camille Viatte[1], Anne Boynard[1,2], François Ravetta[1], Jacques Pelon[1], Cristelle Cailteau-Fischbach[1], Pascal Genau[1], Julie Capo[3], Axel Roy[3], and Philippe Nédélec[4]

[1]LATMOS, Sorbonne Université, Université Versailles St-Quentin, CNRS/INSU, Paris, France
[2]SPASCIA, Ramonville-Saint-Agne, 31520, France
[3]CNRM, Université de Toulouse, Météo-France, CNRS, Toulouse, France
[4]Laboratoire d'Aérologie, CNRS and Université Toulouse III, Paul Sabatier, Toulouse, France

Correspondence: Gérard Ancellet (gerard.ancellet@latmos.ipsl.fr)

Received: 25 March 2024 – Discussion started: 30 April 2024
Revised: 24 September 2024 – Accepted: 24 September 2024 – Published: 25 November 2024

Abstract. The variability of ozone vertical profiles in the Paris area is analyzed using 21 d of lidar monitoring of the lower-troposphere ozone vertical profiles and planetary boundary layer (PBL) vertical structure evolution in summer 2022. Characterization of the pollution regional transport is based on daily ozone analysis of the Copernicus Atmospheric Service (CAMS) ensemble model and on backward trajectories. The CAMS simulations of the ozone plume between the surface and 3 km are consistent with the ozone measurements. Comparisons with the tropospheric ozone column retrieved by satellite observations of the Infrared Atmospheric Sounding Interferometer (IASI) show that IASI observations can capture the day-to-day variability of the 0–3 km ozone column only when the maximum altitude of the ozone plume is higher than 2 km.

The lidar ozone vertical structure above the city center is also in good agreement with the PBL growth during the day and with the formation of the residual layer during the night. The analysis of four ozone pollution events shows that the thickness of the PBL during the day and the advection of regional-scale plumes above the PBL can significantly change the ozone concentrations above Paris. Advection of ozone-poor concentrations in the free troposphere during a Saharan dust event is able to mitigate ozone photochemical production. On the other hand, the advection of a pollution plume from continental Europe with high ozone concentrations $> 140\,\mu\mathrm{g\,m^{-3}}$ maintained high concentrations in the surface layer despite a temperature decrease and cloud cover development.

1 Introduction

Ozone pollution poses significant challenges for air quality management during summer due to its harmful effects on human health and ecosystems (Fowler et al., 2008). As a secondary pollutant, O_3 results from the interaction of sunlight with primary pollutants like nitrogen oxides (NO_x) and volatile organic compounds (VOCs), with summer months being most conducive to its formation (Monks et al., 2015). These interactions are strongly influenced by atmospheric conditions, which vary within the planetary boundary layer (PBL), the part of the atmosphere where the surface emissions directly affect weather and air quality. Vertical profiling of O_3 within the PBL is essential for several reasons. Firstly, the production and destruction of O_3 at different altitudes in the PBL depend on the vertical distribution of precursor chemicals and meteorological conditions (Zaveri et al., 2003). Secondly, vertical transport processes within the PBL, such as turbulent mixing and convective uplift, significantly impact the distribution and concentration of O_3 and its precursors (Seinfeld and Pandis, 2016). Thirdly, the O_3 plume from urban centers in the context of megacities, where large volumes of pollutants are emitted, can be transported across urban scales and can influence regional air quality significantly. For instance, the interplay between local emission sources in large urban areas and regional meteorological patterns can result in the formation of extensive O_3 plumes that affect large geographical regions (Couillard et al., 2021; Ma et al., 2021). The summer 2022 ACROSS (Atmospheric ChemistRy Of the Suburban foreSt) measurement campaign as part of the PANAME (PAris region urbaN Atmospheric observations and models for Multidisciplinary rEsearch) project employed advanced techniques like O_3 lidar, backscatter microlidar, Doppler lidar, radiosounding, and aircraft measurements to characterize the vertical structure of the low troposphere in the Paris city center area. This approach enables us to dissect the complex interactions between O_3, its precursors, and meteorological factors at various altitudes in the PBL. The O_3 data gathered provide insights into the mechanisms driving pollution episodes and aid in the identification of primary factors contributing to high-O_3 events.

Over the past 2 decades several campaigns have focused on understanding O_3 pollution episodes in cities. The “Etude et Simulation de la Qualite de l’air en Île-de-France” (ESQUIF) project was conducted in the Paris region (Vautard et al., 2003), the main focus being the analysis of the contrast between summer and winter conditions in the relative contribution of local O_3 photochemistry compared to regional transport. The ESQUIF campaign results demonstrated that the Paris area was well suited to study the urban heat island (UHI) effect in pollutant distribution due to enhanced turbulence inside the boundary layer (Sarrat et al., 2006). During the ESCOMPTE campaign held in 2001, the focus was on the fate of the Marseille area urban and industrial emissions of O_3 formation in the context of very complex meteorological conditions with land–sea breeze and orographic effects (Drobinski et al., 2007). Ground-based UV differential absorption lidar (DIAL) O_3 and aircraft observations demonstrated the sensitivity of the lowermost tropospheric vertical O_3 distribution to mesoscale dynamical processes (Ancellet and Ravetta, 2005). Several campaigns took place in North America to characterize high O_3 summer concentrations: the Texas Air Quality Study (TexAQS) 2000 and 2006 and the TRacking Aerosol Convection ExpeRiment – Air Quality (TRACER-AQ) 2021 in the southwestern USA (Daum et al., 2004; Senff et al., 2010; Liu et al., 2023), California Research at the Nexus of Air Quality and Climate Change (CalNex), the California Baseline Ozone Transport Study (CABOTS) 2016, the Las Vegas Ozone Study (LVOS) 2016 and 2017 in California (Ryerson et al., 2013; Langford et al., 2022; Faloona et al., 2020), and the Long Island Sound Tropospheric Ozone Study (LISTOS) 2018 and 2019 in New York City (Couillard et al., 2021). During these campaigns aircraft and lidar were extensively used to better understand the sources and formation mechanism of O_3 plumes (Langford et al., 2019). Results of LISTOS, CABOTS, and TRACER-AQ show that meteorology and boundary layer heights are significant parameters influencing the vertical distribution of O_3 in these areas. Sullivan et al. (2017) demonstrated that residual O_3 layer reincorporation with mixed layer development contributes to a significant part of surface O_3 concentration increase in the afternoon. The contribution of the long-range transport of O_3 has also been analyzed using airborne differential absorption lidar (DIAL) and satellites. For example, it was shown that regional transport of O_3 from Asian emissions over the North Pacific Ocean to California is responsible for a significant part of the lower-tropospheric O_3 increase in summer (Lin et al., 2012; Langford et al., 2017) and that stratospheric–tropospheric exchanges (STEs), forest fires, and Asian pollution significantly control baseline ozone and therefore O_3 pollution in urban areas in North America (Langford et al., 2022; Wang et al., 2021; Faloona et al., 2020).

In the present paper the focus will again be on the Paris area, taking advantage of the ACROSS campaign held in summer 2022 with numerous aircraft flights around Paris and several remote sensing lidar and radar observations carried out in June and July. Several O_3 pollution episodes were encountered during this period. The presentation of the O_3 vertical observations available during this period as well as a preliminary analysis of the respective contribution of the urban boundary layer structure and of the O_3 plume regional transport are the main objectives of this paper. The latter has been extensively discussed for the North American campaigns listed above, but it is not clear if similar conclusions can be drawn for the Paris area about the role of elevated ozone concentrations transported from outside the megacity area. The Paris area is also different from places with complicated pollution plume recirculation due to orography or land–sea breeze meteorological forcing, with many previous campaigns taking place in Europe or North America. Therefore it is relevant to present a study specific to the development of ozone pollution in the Paris area.

The overall description of the O_3 variability during the ACROSS campaign and the selection of the pollution events analyzed in this work are presented in Sect. 3.1. This section focuses on lidar observations and the comparison with aircraft and model data. Section 4.1 first shows to what extent the O_3 measurements discussed in this work are relevant for studying the summer day-to-day variability of ozone in the lower troposphere in Paris, including the potential input from satellite observations. Section 4.2 presents the analysis of the regional O_3 transport during ACROSS since this process has been recognized during past campaigns as a significant source of variability. Section 4.3 and 4.4 summarize the main characteristics of the summer pollution episodes encountered during ACROSS and put the results into a broader perspective by comparing them with those of past measurement campaigns.

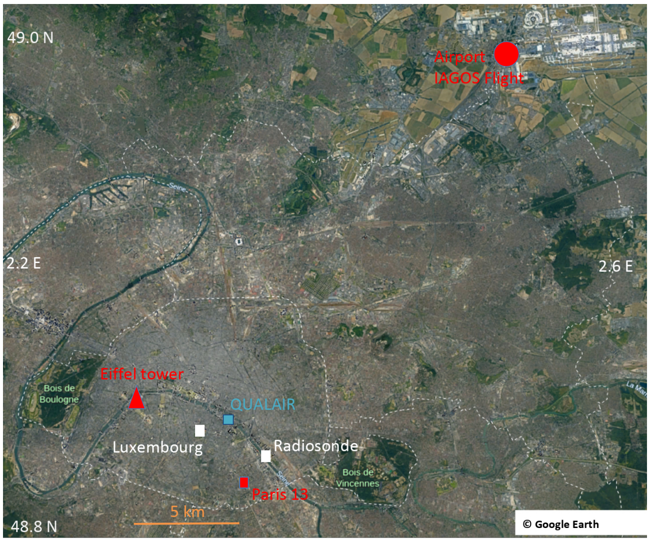

Figure 1. Google Earth map of the Paris area with O_3 and meteorological measurement positions during the ACROSS 2022 experiment. The blue mark is the position of the QUALAIR station including the O_3 DIAL (33 m a.s.l.) and instruments operated on the top of the Zamansky tower (125 m a.s.l.). The red triangle is the Eiffel Tower third platform (310 m a.s.l.), the red square is the AIRPARIF PARIS 13 in situ O_3 monitor in Parc de Choisy (50 m a.s.l.), and the red circle is the IAGOS aircraft take-off and landing airport. White squares show the Luxembourg park surface meteorological station (46 m) and the meteorological radiosounding station.

2 Description of observation and modeling tools

2.1 In situ surface observations

Numerous observations are available in the Paris area to monitor hourly averaged O_3 concentration and temperature. We will focus in this work on three monitoring sites located in (i) the Paris 13 station at 60 m a.s.l. in a park not directly influenced by traffic emissions, (ii) the top of the QUALAIR Zamansky tower at 125 m a.s.l., and (iii) the third floor of the Eiffel Tower at 310 m a.s.l. (Fig. 1). Since no temperature data are available at the Paris 13 station, the Luxembourg park temperature at 46 m a.s.l. has been used to characterize the surface temperature. The accuracy of the O_3 measurements is around 5 $\mu g\, m^{-3}$. O_3 concentrations are provided in $\mu g\, m^{-3}$ by the AIRPARIF air quality network. The tower observations have been used to characterize the temporal evolution of the surface layer lapse rate and the O_3 vertical gradient near the surface. The latter is very useful to measure the O_3 vertical profile down to the ground as the QUALAIR lidar is blind below 250 m a.g.l.

2.2 Ozone vertical profiles

The observations discussed in this work were carried out during the ACROSS campaign from 13 June to 13 July 2022. O_3 vertical profiles are obtained from a UV DIAL instrument installed on the Sorbonne Université campus. The instrument is described in Klein et al. (2017) and Ancellet and Ravetta (1998) and provides observations in the altitude range 0.3 to 5 km during nighttime and up to 2.7 km during daytime. Only daytime measurements were carried out during ACROSS 2022 as the lidar could not be remotely controlled during this campaign. Although the DIAL sampling rate is 15 s, the O_3 vertical profiles are usually hourly averages to match the surface data time resolution and to improve the lidar signal-to-noise ratio above the planetary boundary layer top. The accuracy of the lidar observations is altitude-dependent and of the order of 7 $\mu g\, m^{-3}$ below 1000 m; it occasionally increases up to 20 $\mu g\, m^{-3}$ above 2 km at midday (Klein et al., 2017). The latter is due to elevated background skylight noise at noon or a reduction in the number of averaged lidar shots during scattered cloud occurrence at altitudes below 2 km. The vertical resolution is less than 100 m at a 250 m altitude and of the order of 500 m at a 2500 m altitude. O_3 concentrations will be given in $\mu g\, m^{-3}$ in this paper as it is the true quantity measured by the lidar, and ozone observations made by the air quality network are also given in $\mu g\, m^{-3}$ (conversion to mixing ratio at 25 °C and 1 atm is $1\ \text{ppbv} = 1.96\ \mu g\, m^{-3}$).

Ozone in situ measurements on IAGOS (In-service Aircraft for a Global Observing System) aircraft provide a vertical profile of O_3 during take-off and landing at the Paris Charles de Gaulle (CDG) airport (Nédélec et al., 2015). Typical aircraft trajectories during landings (early morning flights before 06:00 UT) and take-offs (midday flights after 10:00 UT) are shown in the Supplement (Figs. S1, S2). The horizontal domain, where the aircraft remains at altitudes of less than 3 km, does not exceed a radius of 40 km around CDG airport. The aircraft is never above the city center when it flies below 3 km. The aircraft location is generally northeast of Paris between 2.5 and 3° E during take-off (afternoon flights), except on 13 July when the aircraft position was northwest of Paris. The aircraft positions during landing (early morning flights) are generally within a 20 × 50 km box either northwest or northeast of Paris. The accuracy of the IAGOS O_3 measurements is better than ±2 ppbv or ±2 % (Thouret et al., 1998), and the vertical resolution of the O_3 profile is of the order of 30 m. The respective positions of the O_3 DIAL and the CDG airport are shown in Fig. 1.

2.3 PBL height characterization

Two instruments have been used to characterize the PBL evolution near the QUALAIR O_3 lidar: an autonomous 808 nm microlidar (SLIM) derived from the IAOOS instrument developed by CIMEL and LATMOS (Pelon et al., 2008; Mariage et al., 2017) and meteorological radiosondes launched four times a day for 6 d of pollution in June 2022. The SLIM lidar is routinely operated at the Jussieu QUALAIR facility on a 24 h and 7 d basis. It provided observations during the full ACROSS campaign using an automated procedure. In this procedure, the raw backscattered signal is first normalized using the integrated attenuated backscatter signal on water cloud layers (O'Connor et al., 2004). The attenuated backscatter signal is derived from the SLIM lidar signal after calibration and correction of the geometrical factor (Pelon et al., 2008; Mariage et al., 2017). The attenuated backscatter is used to identify clouds on the basis of a lidar signal attenuated backscatter above a predefined threshold ($0.25\,\mathrm{km}^{-1}\,\mathrm{sr}^{-1}$). It is then inverted to derive the backscattering coefficient in aerosol regions using a forward inversion procedure (Klett, 1985). A standard lidar ratio value of 40 sr is used, corresponding to urban aerosol. Further refinements in the analysis can be performed to derive more accurate aerosol and cloud optical properties but are not used here. The analysis is performed on 1 min (the acquisition time) and 10 min files.

The PBL height and the top of the residual boundary layer (RBL or RL, which remains from the previous PBL development) are derived from the vertical structure of the aerosol backscattering coefficient and its variance as markers of the turbulent activity developed in the unstable summer boundary layer (Stull, 1988). A simple approach based on the analysis of the gradients is used following previous studies (Dupont et al., 1994; Flamant and Pelon, 1996; Menut et al., 1999). A combination of information is used to mix backscattering and variance-derived heights in order to identify PBL and RL heights. It requires that significant vertical motions can be identified, as is the case during daytime. The signature of such dynamics in the lidar signal is a coincident variance peak and a backscattering gradient (Menut et al., 1999). In the decay phase, or in the nocturnal layer development, the PBL height can be estimated from the variance as linked to residual turbulence activity (Stull, 1988). The RL height can be derived from the backscattering coefficient gradient, as particles are maintained in the atmosphere close to the maximum height (depending on particle size and subsidence) reached by the PBL during the day (or the day before for the morning period).

The meteorological radiosondes have been used to plot the thermodynamic skew-T diagram in order to determine the depth of the layer limited by the adiabatic ascent. It also allows capturing the lifting condensation level (LCL) where cloud base can be expected and the level of free convection (LFC) above which fast vertical motion and deep convection can occur. The Python library metpy.calc.lcl has been used for the automatic retrieval of LFC and LCL. It is complementary to the SLIM estimate of the PBL vertical structure. The SLIM lidar and the radiosounding site locations are shown in Fig. 1.

2.4 Satellite observations: IASI

The IASI (Infrared Atmospheric Sounding Interferometer) is a nadir-viewing spectrometer (Boynard et al. 2009) that records the thermal infrared emission of the Earth–atmosphere system between 645 and $2760\,\mathrm{cm}^{-1}$ from the polar Sun-synchronous orbiting meteorological Metop series of satellites. Metop-A, Metop-B, and Metop-C were successively launched in October 2006, September 2012, and November 2018. IASI provides global coverage of the Earth twice a day (at 09:30 and 21:30 mean local solar time) with a set of four simultaneous footprints of 12 km diameter on the ground at nadir. Thanks to the IASI high spectral resolution of $0.5\,\mathrm{cm}^{-1}$ and low radiometric noise below 0.4 K, the vertical composition of various trace gases such as O_3 can be assessed in the troposphere (Eremenko et al., 2008; Boynard et al., 2009; Viatte et al., 2011; Safieddine et al., 2013; Wespes et al., 2018).

In this study, we use the IASI O_3 profiles retrieved from the FORLI (Fast Optimal Retrievals on Layers for IASI) algorithm (Hurtmans et al., 2012). The FORLI O_3 products (profiles and columns) have undergone a series of validation using available ground-based, aircraft, ozonesonde, and other satellite observations over local areas and/or short time periods (Antón et al., 2011; Dufour et al., 2010; Pommier et al., 2012) and more recently at a global scale over a 10-year period (Boynard et al., 2016, 2018; Keppens et al., 2018). IASI data and ozonesonde measurements are in agreement in the troposphere at midlatitudes (differences of 11 %–13 %), with significant vertical sensitivity in the troposphere (Boynard et al., 2018). For this work, IASI as well as Metop-B and Metop-C pixels located within the ACROSS domain (48.84–49° N, 2–2.5° E) associated with a fractional cloud coverage of 13 % or less and filtered by retrieval quality flags (see Boynard et al., 2018) have been selected. The O_3 0–3 km partial columns can be retrieved for both morning (≈ 09:30 LT) and evening (≈ 21:30 LT) overpasses.

2.5 CAMS ozone plume modeling

The Copernicus Atmosphere Monitoring Service (CAMS) provides ENSEMBLE model hourly analysis of O_3 and NO_2 concentration at five levels (500, 750, 1000, 2000, 3000 m) with a horizontal resolution of 10 × 10 km. Up to 11 air quality models are used to build the ENSEMBLE analysis, reducing the sensitivity to model error (Marécal et al., 2015; Inness et al., 2019). In this work analyses have been used at three daily time steps of 06:00, 12:00, and 18:00 UT to map the O_3 and NO_2 plume positions over northern France. The quality of the tropospheric O_3 CAMS daily analysis is generally in good agreement with ozonesondes and IAGOS aircraft observations at northern midlatitudes, especially in simulating the formation of regional O_3 plumes during the summer (Wagner et al., 2021).

3 The ACROSS ozone vertical profile dataset

3.1 Selection of the ozone measurement period

The ACROSS 2022 campaign took place during three interesting periods with O_3 concentrations above 100 µg m^{-3} and surface temperature above 30 °C. The time evolution of the surface hourly O_3 and temperature means is shown in Fig. 2 for the three stations located at different altitude levels between 40 and 310 m a.s.l. The 12 d corresponding to the red arrows in Fig. 2 have been chosen to determine how the characterization of vertical O_3 profiles and the spatial distribution of the pollution plume on a regional scale can be used to better intercompare these different O_3 pollution episodes. Unfortunately no lidar data are available after 14 July, e.g., during the O_3 pollution episode on 18 July. This is why this last pollution event is not considered in this work. The 500 m CAMS O_3 distribution is a good proxy to track the day-to-day spatial distribution of the O_3 plume at the regional scale, this plume being related to both the regional emissions from western Europe and urban emissions from the Paris area. They are shown at 18:00 UT when O_3 concentrations reach their daily maximum in Figs. 3 and 4 for the 12 d identified in Fig. 2. The first period with elevated O_3 concentrations took place from 14 to 18 June. This period was characterized by the highest O_3 concentrations (170 µg m^{-3}) recorded within the city center, but also by O_3 concentrations > 140 µg m^{-3} over a large fraction of northern France according to the CAMS simulations (Fig. 3). The second time period from 21 to 28 June is rather typical of summer sunny days with ground temperatures near 30 °C and moderate O_3 pollution of the order 110 µg m^{-3} on 21, 22, and 28 June. The CAMS simulations show a well-defined O_3 plume west of Paris on 21 and 22 June (Fig. 4a, b) with O_3 concentrations approaching 150 µg m^{-3}. 28 June is also interesting as the Paris O_3 concentrations below 300 m are similar to the 21–22 June episode, while the 28 June CAMS O_3 concentrations in the plume located north of Paris (Fig. 4c) remain below 130 µg m^{-3}. The third O_3 pollution period took place on 11 until 13 July with regional O_3 plumes (Fig. 4d, e, f) somewhat similar to the 21–22 June case study. The city center O_3 concentrations, however, are as high as 140 µg m^{-3}, approaching the values encountered during the 14 and 18 June episode. Both the O_3 and temperature vertical gradient between the surface and 300 m at the time of the daily maximum decrease on the last days of each pollution episode. Measuring the O_3 vertical profiles with the UV DIAL and IAGOS aircraft above the top of the Eiffel Tower is mandatory to understand to what extent the structure and intensity of the O_3 plume described by the CAMS simulations can explain the surface measurements in central Paris. A better understanding of the weakening of the surface O_3 vertical gradient between 0 and 300 m altitude will also benefit from lidar and aircraft observations at altitudes above 300 m.

3.2 Boundary layer diurnal variation

An O_3 layer is generally observed during the morning hours above the nocturnal surface layer in the RL (Neu et al., 1994; Klein et al., 2019). It is generally an O_3 reservoir with limited NO_x titration and O_3 deposition. This O_3-rich air in the RL can be mixed down into the surface boundary layer effectively (Caputi et al., 2019). The analysis of the boundary layer height diurnal variation using the microlidar SLIM is necessary to characterize the PBL growth during the day and the downward mixing of the RL. The diurnal variations of the 10 min aerosol backscatter vertical profiles measured by SLIM are shown in Figs. S3 to S6 for the 12 d with elevated O_3 concentrations. The PBL height (PBLH) and RL height (RLH) are derived using the methodology described in Sect. 2.3 and are shown using a blue star and blue circle, respectively, in the Supplement (Figs. S3 to S4). These plots are also useful to identify the occurrence of long-range transport of aerosol plumes in the free troposphere above the PBL, e.g., the Saharan dust plumes observed in the 2–4 km altitude range from 15 to 18 June (Figs. S3b, S4a, b) and the recirculation of European continental aerosol (Fig. S5a, b). The aerosol plume attribution was based on a linear 532 nm depolarization ratio larger than 0.2 measured by the CIMEL lidar measurements of the QUALAIR station and based on the long-range transport modeling in Sect. 4.2. Another interesting feature is the overall difference of the aerosol backscatter magnitude within the PBL when looking at the first (15–18 June) and at last (12–13 July) heat wave episode. The latter, with no dust plume aloft, corresponds to less aerosol backscatter within the PBL. Large 808 nm aerosol backscatter values above 0.01 km^{-1} sr^{-1} (yellow pixels in Figs. S3 to S6) correspond to cloud layer formation at the top and above the PBL. The 1 min high-resolution cloud observations of the SLIM lidar have also been used to filter out the cloudy DIAL observations when retrieving the O_3 profile.

Data from the 16 meteorological radiosondes are also shown in Table 1 and in Figs. S3 to S5 using thermodynamic skew-T diagrams. The bottom altitudes of inversion layers (ILHs) detected by the radiosondes below 4 km shown in Table 1 are retrieved using layers with potential temperature vertical gradient larger than 15 K km^{-1}. They can be compared with the SLIM PBLH and RLH. There is good agreement between the lidar retrieval and the analysis of the meteorological radiosondes, especially for the timing of the PBL growth and the low thickness of the surface layer around 00:00 UT. The PBLHs generally remain below 2 km between 14 and 22 June (Figs. S3 to S5b), except on 18 June with a fast rise of the PBLH in the evening (Fig. S4b). The PBLHs, however, exceed the 2 km altitude level on 28 June (Fig. S5c) and during the third pollution episode (Fig. S6). It is likely related to a change in the atmospheric circulation due to a change in synoptic weather pattern, with anticyclonic downward advection before 22 June and upward advection of marine air from the Atlantic Ocean and the North Sea on 28 June

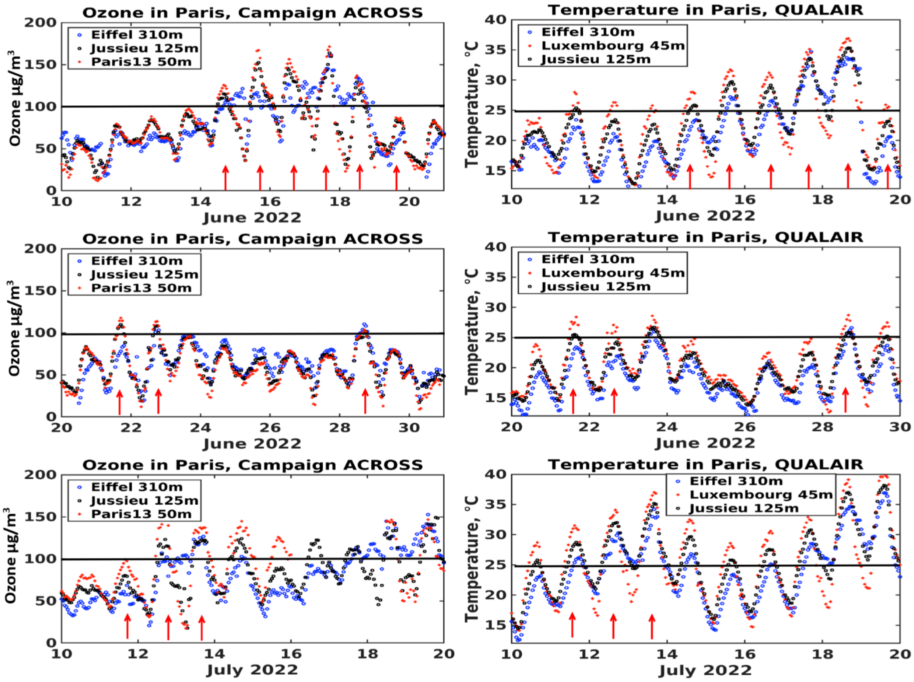

Figure 2. Surface O_3 concentration and temperature 10 d time evolution of the hourly mean during the ACROSS 2022 campaign in blue for the Eiffel Tower top (310 m a.s.l.), in black for the Zamansky tower top (125 m a.s.l.), and in red for the Paris 13 O_3 sensor and for the Luxembourg park meteorological station (50 m). Days selected for the analysis of O_3 pollution events are shown by the red arrows.

Table 1. Comparison of the 808 nm microlidar SLIM planetary boundary layer (PBL) and residual layer (RL) heights with the meteorological radiosounding inversion layer (IL) bottom altitudes observed below 4 km.

Date (mm/dd)	06/14	06/16		06/17			06/18			06/19	06/22			06/28		
Hour, UT	00:00	12:00	20:00	00:00	12:00	20:00	00:00	12:00	20:00	00:00	12:00	16:00	20:00	00:00	12:00	20:00
First IL height, km	0.2	1.4	1.6	0.2	1.2	0.25*	0.2	1.0	0.3*	0.5	0.5*	0.8	1.0	0.4	2.1	2.3
Second IL height, km	1.4		2.2			1.2		3.5	3.5	3.5	1.5*	2.0	3.8	2.4		
Lidar PBL height, km	0.3	1.3	1.0	0.25	1.2	0.5	0.25	1.0	3.5	0.25	0.7	0.9	1.0	0.4	2.1	1.6
Lidar RL height, km	1.5		1.7	1.2		1.1	1.02			3.5			1.9	2.2		2.3

* Stable layer with thickness < 50 m.

and on 11 to 13 July (see Sect. 4.2). The largest PBLHs beyond 3 km were observed on 18 June and 13 July for the highest surface temperatures above 35 °C (Fig. 2).

The daily maximum of the PBLH generally occurs around 17:00 UT, while PBLH and RLH decrease below 2 km at 23:00 UT despite high surface temperatures. Another interesting feature for the downward transport of O_3 the following day is the occurrence of RL heights below 1.5 km at 21:00 UT, followed by a continuous decrease in RLHs after 21:00 UT. There are 4 d with such behavior: 14, 16, and 22 June and 12 July. These 4 d in fact correspond to high nighttime surface O_3 concentrations above 100 $\mu g\,m^{-3}$ (Fig. 2), consistent with an efficient downward mixing of RLs in the 0–300 m surface layer during the night.

3.3 DIAL ozone diurnal variation

The O_3 vertical profiles are taken from the O_3 DIAL observations for the days selected in Sect. 3.1. The time–altitude daytime evolution of the O_3 concentration is shown in the left-hand columns of Figs. 5 and 6. Data from the surface stations shown in Fig. 2 are also included in these figures using the same color-coded scale. They correspond to the pixels with the black cross in Figs. 5 and 6. The diurnal

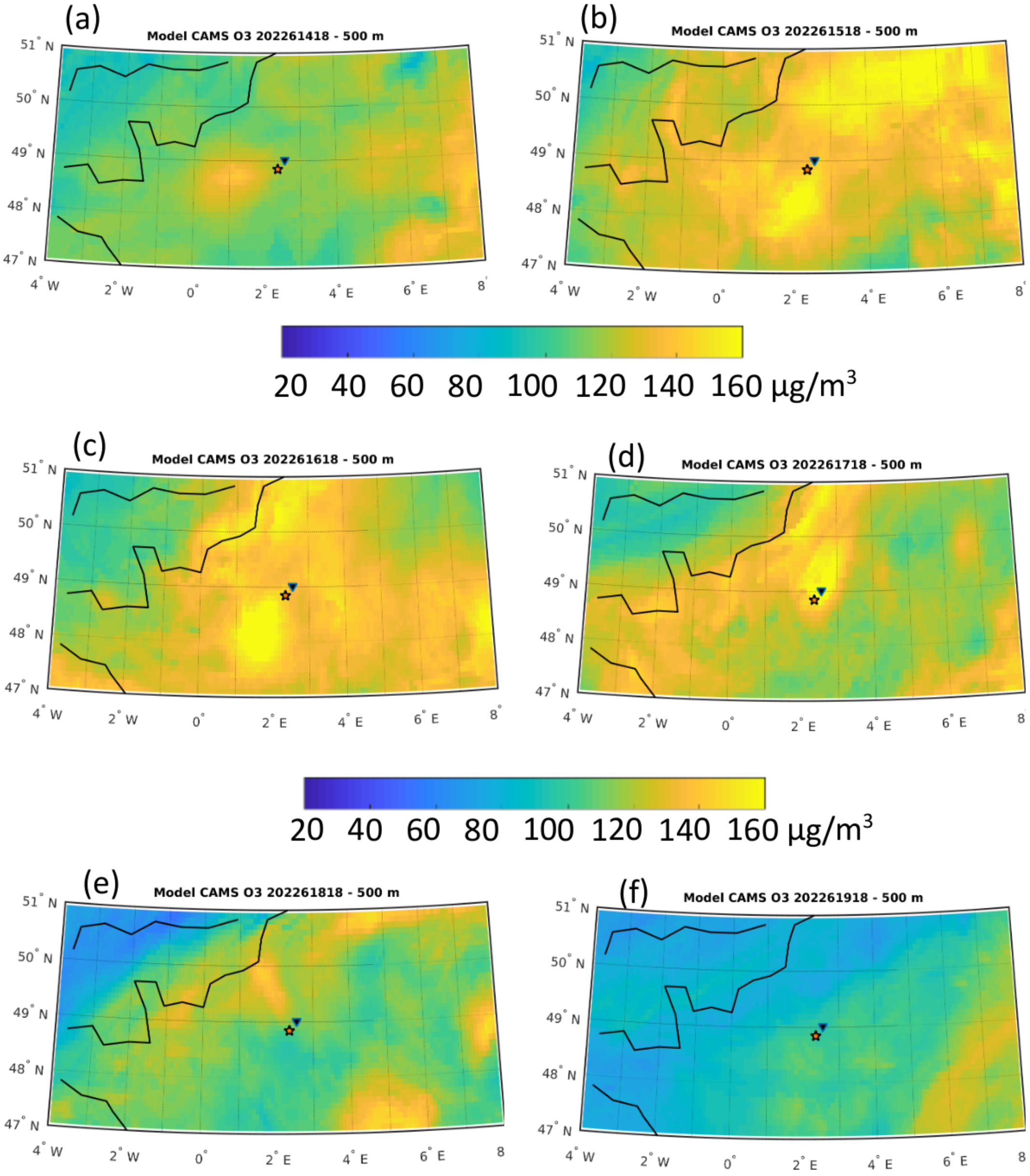

Figure 3. Ozone concentration distribution of the CAMS ensemble mean at 500 m above northern France from 14 June **(a)** to 19 June **(f)** 2022 at 18:00 UT. The orange star and dark-blue triangle are respectively the DIAL position and the CDG airport. The color scale represents the O_3 concentration in µg m^{-3}.

cycle observed by the Eiffel and Zamansky tower stations at 125 and 310 m is consistent with the lidar observation at 300 a.s.l., following the previous study of Klein et al. (2017). CAMS vertical O_3 profiles are also retrieved using the ensemble model data at five vertical levels and within the box [48.84–49° N, 2–2.5° E]. The latter corresponds to a horizontal domain of 36 km × 17 km including the QUALAIR station and the CDG airport. The CAMS vertical profiles are shown at 06:00, 12:00, and 18:00 UT in Fig. 7 when DIAL observations are available. The averages of the morning and midday IAGOS O_3 vertical profile up to 3 km are also shown in Fig. 7. The averages of the morning and midday DIAL O_3 profiles are also shown for the time periods of the IAGOS flights in Fig. 7. Such a comparison of the three O_3 profiles is useful to check if the O_3 layers observed by the DIAL in the Paris city center are also present at the scale of the entire Paris Ile de France region and if advection of the regional O_3 plume plays a significant role in the O_3 diurnal variation in the city center. The PBLH and RLH diurnal variation derived from the results of Sect. 3.2 is also included in the DIAL O_3 time–altitude cross-sections (Figs. 5 and 6) to take into account the role of RL in the O_3 vertical profile diurnal varia-

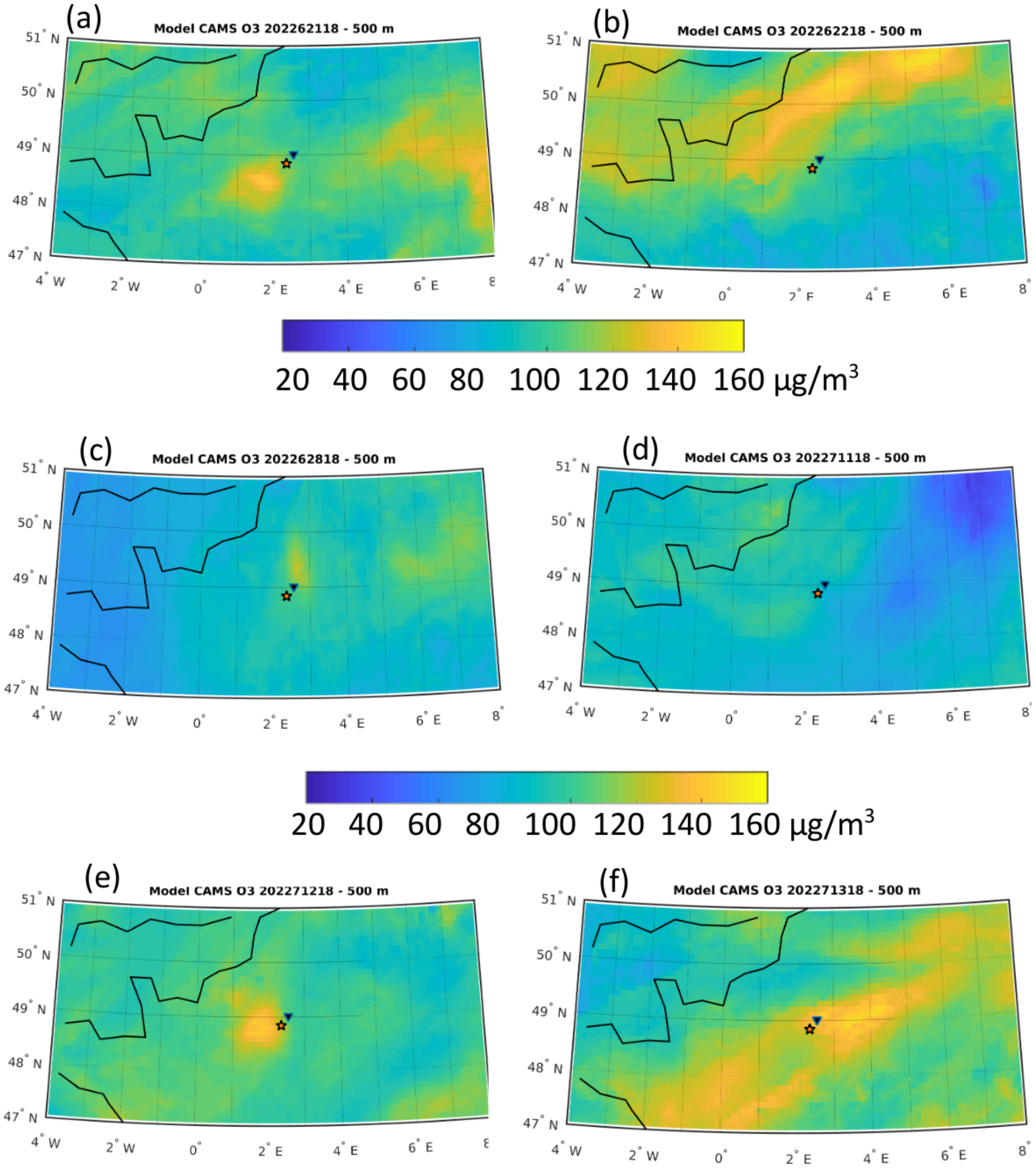

Figure 4. As Fig. 3 for 21 June **(a)** to 22 June **(b)**, 28 June **(c)**, and 11 July **(d)** to 13 July **(f)** 2022.

tion, but also the possible downward mixing within the PBL of O_3-rich or O_3-poor layers advected in the free troposphere above western Europe.

The well-known early morning O_3 depletion due to the nighttime O_3 deposition and NO_2 titration (Güsten et al., 1998) is observed up to 750 m by the DIAL with concentrations as low as 40 µg m^{-3} before 09:00 UT. The daily maximum O_3 concentrations at the surface and the PBL top are always found after 14:00 UT when O_3 precursor gases are transported upward within the PBL. The largest daily O_3 concentrations (up to 175 µg m^{-3}) in the 500–1000 m altitude layer observed by the DIAL on 15 to 17 June correspond very well to the 3 d when elevated CAMS O_3 concentrations larger than 140 µg m^{-3} are present over a large part of northern France according to Fig. 3. The IAGOS and CAMS vertical profiles in Fig. 7 also show that the largest O_3 concentrations are observed below 1.5 km over the Paris Ile de France area (150–160 µg m^{-3}) on 16 June. The 2 d with the lowest UV DIAL O_3 concentration (below 100 µg m^{-3}) on 28 June and 11 July corresponds to a large fraction of northern France with O_3 daily maximum at 18:00 UT below 80 µg m^{-3} (Fig. 4c, d). The IAGOS and CAMS O_3 vertical profiles also show concentrations below 100 µg m^{-3} for these 2 d (Fig. 7).

The depth of the afternoon O_3 layer is generally below 1.5 km and corresponds quite well to PBLH (blue star in

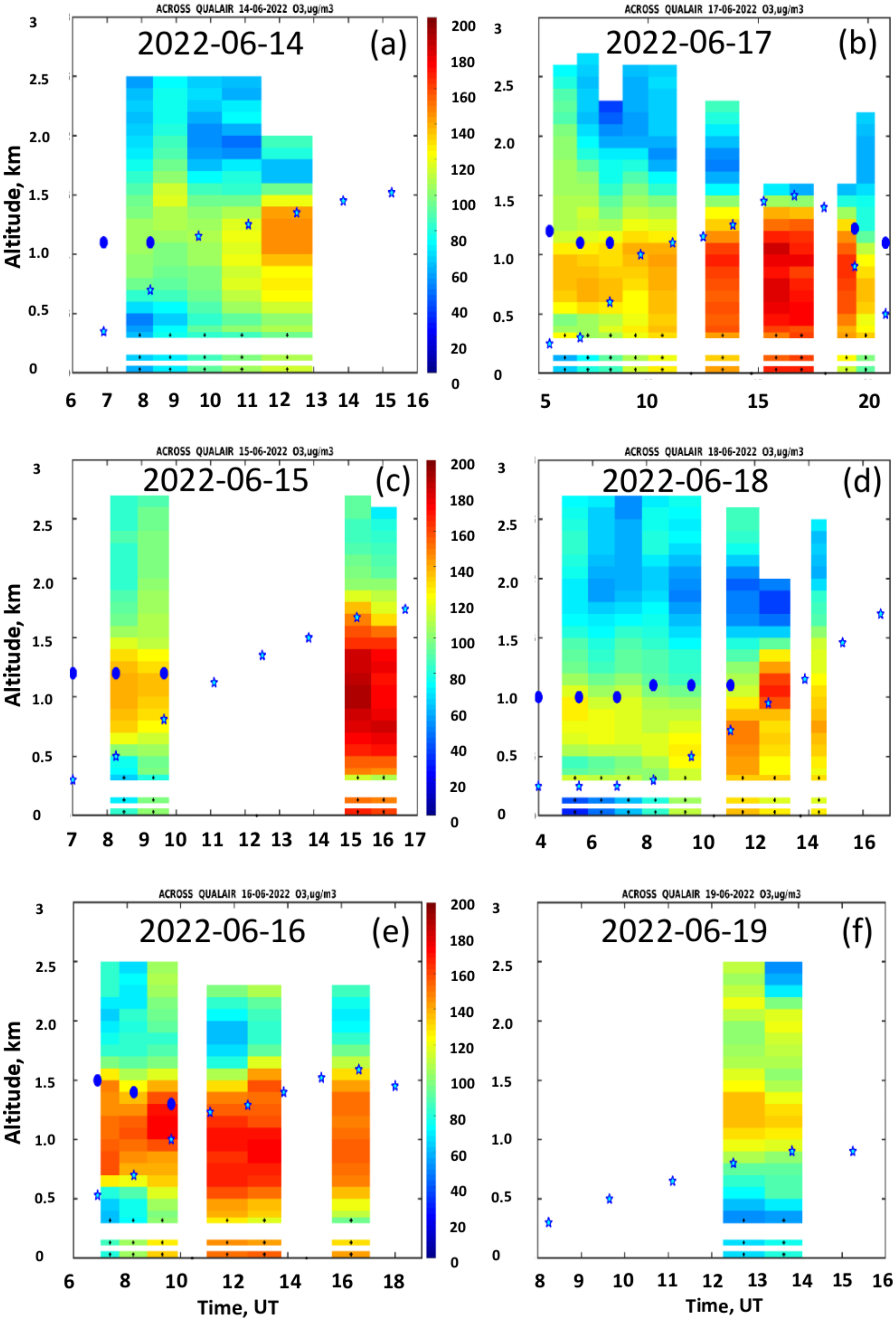

Figure 5. Time–altitude O_3 concentration daytime evolution in $\mu g\, m^{-3}$ from 14 to 19 June 2022 using DIAL above 300 m and the in situ O_3 monitor below 300 m (pixel with black cross). The blue star and circle are the SLIM lidar PBLH and RLH shown in the Supplement.

Figs. 5, 6), except on 19 and 22 June when the O_3 layer extends up to 1.5 km while the PBLH maximum remains below 1 km. On 22 June, PBLH might be underestimated by SLIM since, on one hand, PBLH retrieved in Sect. 3.2 rises up 2 km only after 17:00 UT despite the presence of an aerosol layer up to 2 km at 15:00 UT and, on the other hand, the 16:00 UT meteorological sounding identifies a well-defined ILH at 2 km. The O_3 DIAL might help to clear up ambiguity about the PBLH value more in line with the 16:00 UT radiosounding. On 19 June, there is no reason to question the low PBLH of the microlidar SLIM, while advection of the continental pollution plume above the PBL might very well explain the presence of the 130 $\mu g\, m^{-3}$ O_3 layer between 1 and 1.5 km (see Sect. 4.2). There are only 3 d with both PBLH and DIAL O_3 layer depth above 2 km: 28 June

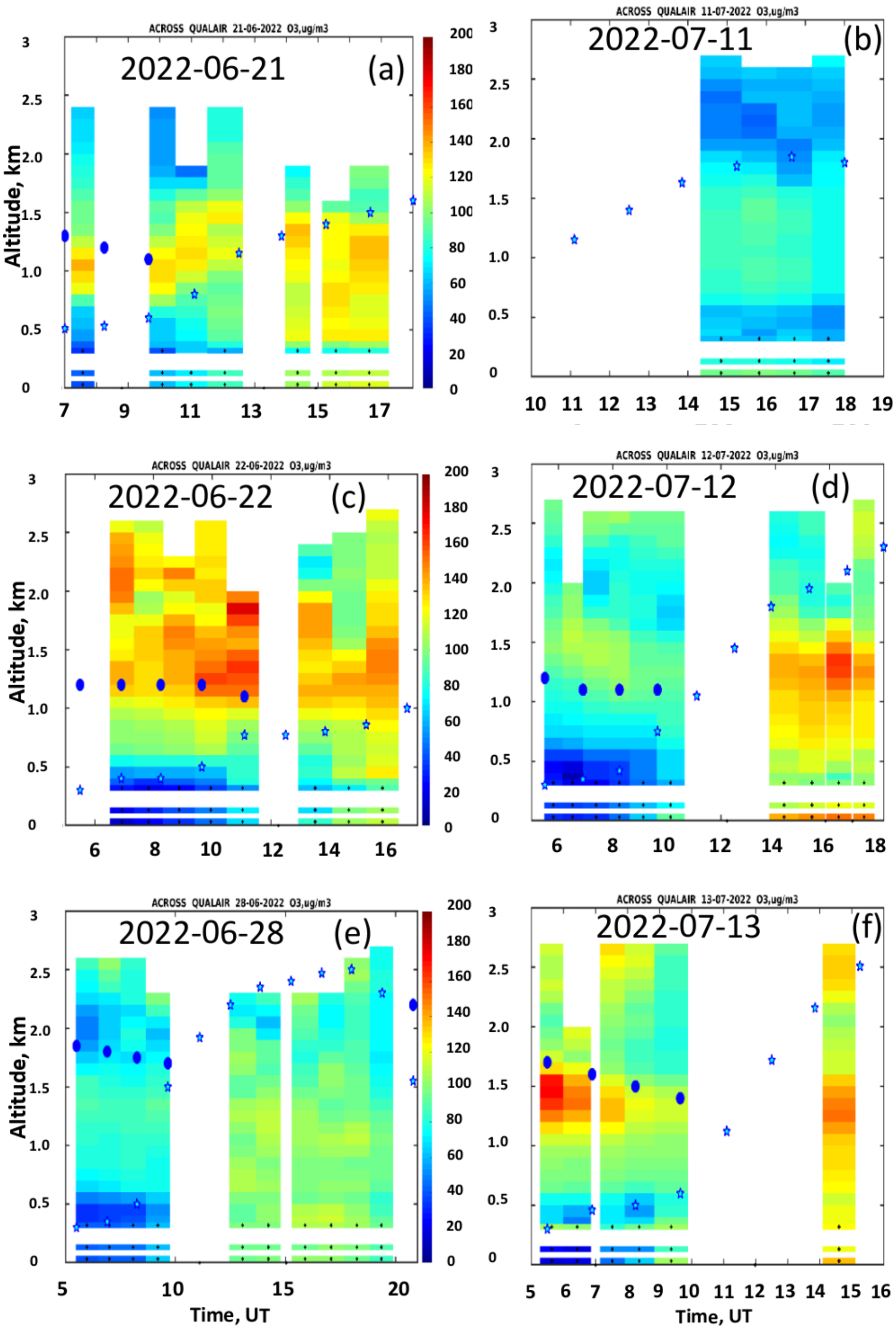

Figure 6. As Fig. 5 for O_3 concentration daytime evolution in $\mu g\,m^{-3}$ for 21, 22, and 28 June 2022 and from 11 to 13 July 2022.

and 12–13 July. The IAGOS O_3 concentrations also reach $100\,\mu g\,m^{-3}$ above 2.0 km on these 3 d (Fig. 7).

The positions of the RLH (blue circle in Figs. 5 and 6) are also in very good agreement with O_3 concentrations above $100\,\mu g\,m^{-3}$ early in the morning between 0.6 and 1.3 km, when high ozone concentrations $> 120\,\mu g\,m^{-3}$ are observed in the PBL on the previous day. Regarding the layers at altitude levels above the PBLH or the RLH, there are two periods with large differences in O_3 concentrations ($\approx \pm 60\,\mu g\,m^{-3}$) measured in the free troposphere and in the PBL and RL. First, low O_3 concentrations less than $80\,\mu g\,m^{-3}$ are observed by the DIAL above 1.5 km on 17 and 18 June (Fig. 5b, d), corresponding to the dust plume advection discussed in Sect. 3.2. The IAGOS and CAMS vertical profiles above 2 km (Fig. 7) also show O_3 concentrations less than $80\,\mu g\,m^{-3}$. Second, the 22 June O_3 layer in the 1–2.5 km altitude layer (Fig. 6c) is different from the other days, with free-tropospheric O_3 concentrations up to

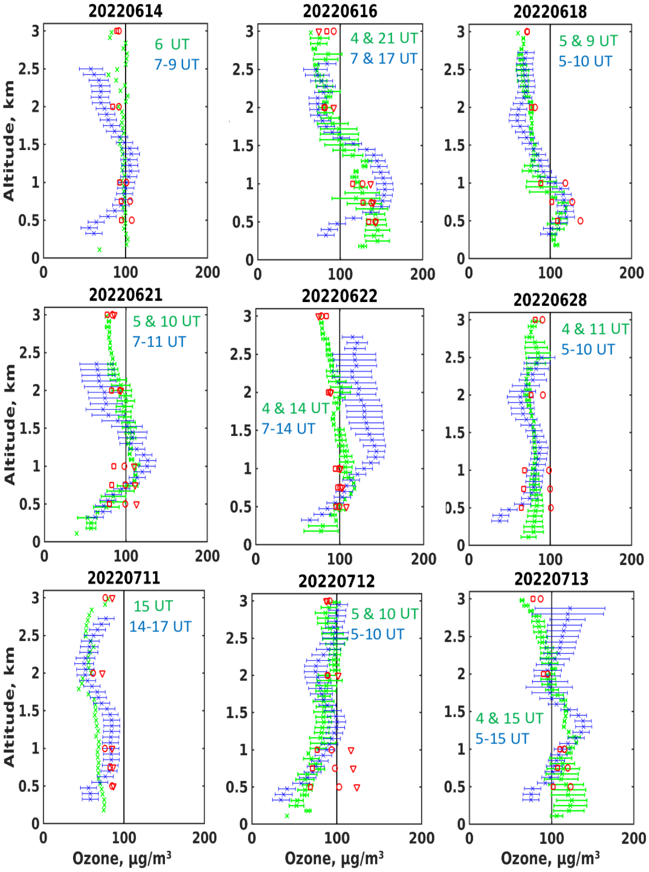

Figure 7. Daily mean O_3 vertical profiles in µg m^{-3} for the IAGOS aircraft (green) and the corresponding DIAL observations (blue) shown in Figs. 5 and 6. Green times in UTC labeled within the figures are the IAGOS measurement times above Paris (two profiles per day except on 14 June and 11 July). Blue times below the IAGOS flight times show the selection of the DIAL observations. CAMS model vertical profiles are also shown using horizontal averages of the model concentrations included in the Fig. 1 area. CAMS profiles are shown at 06:00 UT (red □), 12:00 UT (red ∘), and 18:00 UT (red ▿).

130 µg m^{-3}, while this layer does not mix very well with the surface layer during the day. Such a layer with a concentration larger than 100 µg m^{-3} is not present in the CAMS vertical profile (Fig. 7) above the Paris area. The daily average IAGOS profile on 21 and 22 June also exhibits O_3 concentrations $>$ 100 µg m^{-3} at 2 km (Fig. 7), but this is less than the daily average of the city center DIAL O_3 observations at 2 km on 22 June. This will be discussed in the next section when the regional transport of air masses over Paris is described.

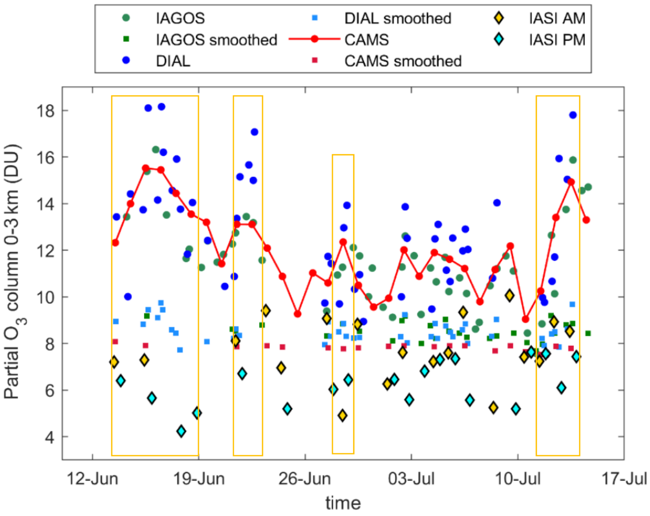

Figure 8. Comparison of the 0–3 km O_3 tropospheric column derived from the ACROSS observations (DIAL in blue and IAGOS in green), CAMS data (in red), and IASI satellite observations (morning – yellow diamonds; evening – cyan diamonds) calculated in the [48.84–49° N, 2–2.5° E] box between 13 June and 13 July 2022. Circles and squares correspond to the 0–3 km O_3 partial column and smoothed partial columns degraded to the IASI vertical resolution, respectively. The orange boxes show the pollution days discussed in Sect. 3.

4 Analysis of the day-to-day variability

4.1 O_3 lowermost tropospheric column: IASI, CAMS, and ACROSS vertical profiles

The IASI O_3 0–3 km partial columns are computed for the period 13 June–13 July 2022 for both morning and afternoon overpasses. Comparisons between IASI O_3 0–3 km partial column, ACROSS observations (IAGOS and DIAL), and CAMS simulations are shown in Fig. 8. All measurement days, whether or not they corresponded to pollution episodes, are considered in order to assess O_3 variability in the lowermost column during the ACROSS campaign from 13 June to 14 July. All the hourly means of the DIAL and IAGOS observations made between 06:00 and 20:00 UT have been considered as well as the IASI morning and evening observations. The daily mean of the columns derived from the CAMS ensemble simulations are shown by the solid red lines in Fig. 8.

For the comparison of IASI data against IAGOS, DIAL, and CAMS data in the ACROSS domain, a temporal coincidence criterion of ±6 h is used. For a proper comparison, the IASI averaging kernels (AKs) are applied to the IAGOS, DIAL, and CAMS vertical profiles in order to account for the differences in vertical resolution and to remove the dependency of the comparison on the a priori O_3 profile information used in the retrieval (Rodgers and Connor, 2003). The IAGOS, DIAL, and CAMS profiles ranging from the surface to 3 km are first interpolated on the IASI vertical grid (which

Table 2. Mean and standard deviation of O_3 partial columns (0–3 km) in Dobson units (DU) derived from IAGOS, DIAL, CAMS, and IASI datasets during the ACROSS campaign between 13 June and 13 July 2022.

Dataset	Raw	Number of observations	Smoothed	Number of observations
IAGOS	11.56 ± 1.93	49	8.53 ± 0.40	28
DIAL	12.88 ± 2.38	52	8.55 ± 0.49	42
CAMS	12.00 ± 1.77	32	7.83 ± 0.12	19
IASI morning	7.75 ± 1.37	19		
IASI afternoon	6.25 ± 0.98	19		
IASI	7.00 ± 1.40	38		

corresponds to 0.5, 1.5, and 2.5 km levels) and then degraded to the IASI vertical resolution by applying the IASI AKs and a priori O_3 profile according to Rodgers (2000):

$$x_s = x_a + \mathbf{A}(x_{raw} - x_a), \tag{1}$$

where x_s is the smoothed IAGOS, DIAL, and CAMS profile; x_{raw} is the IAGOS, DIAL, and CAMS profile interpolated on the IASI vertical grid; x_a is the IASI a priori profile; and $\mathbf{A}$ is the IASI AK matrix. Incomplete IAGOS, DIAL, and CAMS profiles above 3 km are filled with the a priori profile. Based on these criteria, 28, 42, and 19 pairs of observations are found between IASI and the smoothed IAGOS, DIAL, and CAMS data (Table 2), respectively. Over the 13 June–13 July 2022 period, the averaged IASI column of 7.00 ± 1.40 DU is in agreement with the smoothed IAGOS, DIAL, and CAMS datasets, with averaged columns of 8.53 ± 0.40, 8.55 ± 0.49, and 7.83 ± 0.12 DU, respectively.

Figure 8 shows that the O_3 0–3 km partial columns and variabilities derived from IAGOS, DIAL, and CAMS smoothed data are systematically lower than those calculated without taking into account the IASI averaging kernels. Smoothing with the IASI AKs reduces ozone columns and variability because part of the signal information comes from the a priori profile, which is constant over time. However, IASI observations exhibit a variability of ≈ 5 DU (mean of 7.00 ± 1.40) over Paris during the ACROSS campaign, demonstrating that atmospheric signal is present in the retrieval information content with an averaged degree of freedom for signal (DOFS) of 0.22 and 0.08 for morning and evening measurements, respectively. IASI O_3 columns are overall lower than IAGOS, DIAL, and CAMS raw and smoothed columns, with biases of the order of 1–3 DU, in particular when ozone partial columns above 2 km are low, such as between 14 and 19 June and between 29 June and 5 July. Inversely, IASI and the smoothed IAGOS and DIAL O_3 columns are similar in the case of a high PBL (> 2.5 km) or in the case of high ozone above 2 km ($> 100\,\mu g\,m^{-3}$), which is the case on 22 June, 28 June, and 12 July.

DIAL measurements show that the diurnal variability of O_3 0–3 km partial column reaches 5 DU during the ACROSS campaign (blue dots and squares in Fig. 8), confirming the importance of monitoring O_3 profiles at high temporal resolution throughout the day. The day-to-day variability of AM IASI columns is of the same order of magnitude as that of O_3 IAGOS, DIAL, and CAMS raw O_3 columns (5 DU).

4.2 Regional transport of the ozone layer

The potential emission sensitivity (PES) of a passive air tracer is calculated with the FLEXPART model version 9.02 initialized with the 1° × 1° ECMWF operational meteorological analysis (Stohl and Seibert, 1998; Stohl et al., 2002). The FLEXPART model is run backward over 72 h with 17 000 particles released in boxes 35 km by 35 km wide at different altitude ranges above the DIAL: 0–500 m, 0.5–1.2 km, 1.2–2.1 km, and 2.1–3.0 km. The 0.5–1.2 and 2.1–3.0 km PES maps are shown in the Supplement (Figs. S7 to S10) using a color scale in seconds for the vertically integrated residence time of the released particles. One example of the PES maps is shown in Fig. 9. All the grid cell altitudes below 3 km are cumulated to calculate the mean PES in the lowermost troposphere. The NO_2 plume CAMS simulations at the 1 km altitude have been also examined in addition to the O_3 CAMS analysis in order to identify the positions of the Paris plume and the spatial extent of the O_3 pollution plume produced at a wider scale (Fig. 10). The 1° × 1° horizontal resolution of the ECMWF wind analysis is obviously limited for fine tracking of the city plume, but the PES FLEXPART distributions remain very accurate to check to what extent long-range transport must be taken into account in the analysis of the city plume. Looking at the midday PES distributions of particles released either from the PBL or from the free troposphere and then the CAMS simulations, one can distinguish five horizontal advection patterns.

- On 14 and 15 June, advection of continental air masses from Benelux and Germany below 1.2 km transport polluted air over Paris, since the CAMS simulations (Fig. 3) show high-O_3 plumes over these regions. The anticyclonic circulation below 2 km is also consistent with a low PBLH observed in Paris during this time period. Moderate O_3 concentrations in the free troposphere are also consistent with a completely different

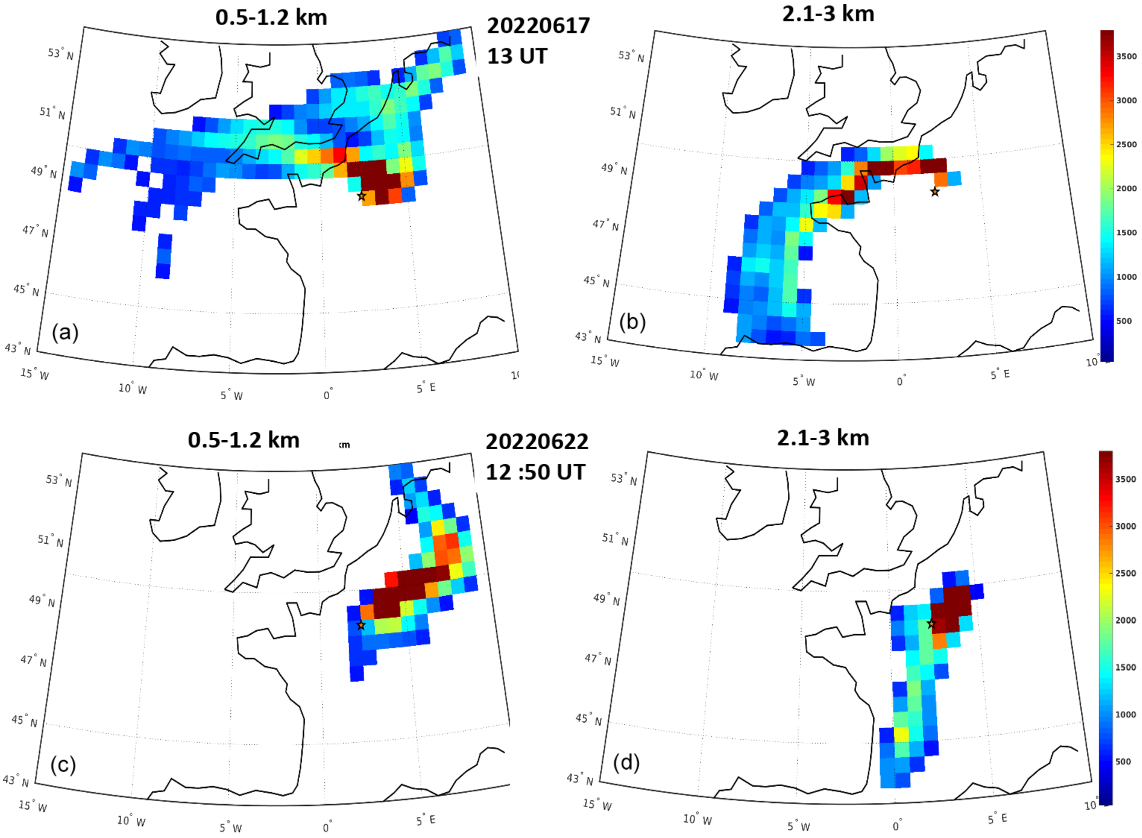

Figure 9. Maps of the vertically integrated FLEXPART backward potential emission sensitivity (PES) for particles released at midday in the 0.5–1.2 km altitude range **(a, c)** and in the 2.1–3 km altitude range **(b, d)** above the DIAL in the Paris city center on 17 June **(a, b)** and 22 June **(c, d)**. The PES color scale is in seconds. Integration time is 3 d. The orange star is the DIAL position.

circulation pattern above 2 km bringing cleaner air from the Atlantic Ocean and the English Channel.

- On 16 to 18 June, in addition to the remaining anticyclonic conditions in the lowermost troposphere, long-range transport of Saharan dust across Spain and the Atlantic coast above 2 km (Figs. 9, S7, and S8) is consistent with a dust aerosol plume just above the PBL measured by the SLIM lidar (Sect. 3.2). The NO_2 plume CAMS simulations (Fig. 10) also show the advection of the low-O_3 streamer located over Brittany and the English Channel on 16 June and east of Paris on 17 June. The low-O_3 layer measured by the DIAL above 1.5 km in Paris is indeed a regional feature not specific to the Paris city center. This southern advection above the PBL also contributes to the chemical composition of the PBL as there is a convergence of two streamers in the PES distribution below 1.2 km (Fig. 9, Fig. S7 bottom row, and Fig. S8 top row). On 18 June, there is no longer any difference in the PBL and the free-troposphere circulation pattern (Fig. S4 middle row), in phase with the growing contribution of the dust plume in the PBL aerosol lidar backscatter (Fig. S4b) and the decrease in ozone in the PBL (Figs. 7 and 5d).
- On 19 to 22 June, the origins of the air masses observed in Paris remain located in eastern France with limited long-range advection in both the PBL and the free troposphere. This is consistent with an aerosol plume of European continental pollution observed by the SLIM lidar on 21 June (Fig. S5a) as well as the advection of the NO_2 continental plume and corresponding high O_3 concentrations from eastern to western France on 22 June (Fig. 10). The low NO_2 concentrations east of the city center in the CAMS simulation (Fig. 10) also explain the positive differences observed on 22 June between the city center DIAL and the IAGOS in situ observations (Fig. 7) when the aircraft was flying east of Paris (Fig. S2).
- On 28 June, the influence of continental air masses is very limited in both the PBL and the free troposphere, while a well-defined westerly flow controls the chemical composition according to the elevated PES values above the Atlantic Ocean (Fig. S9 bottom row). Such a circulation pattern explains both the elevated PBLH (no

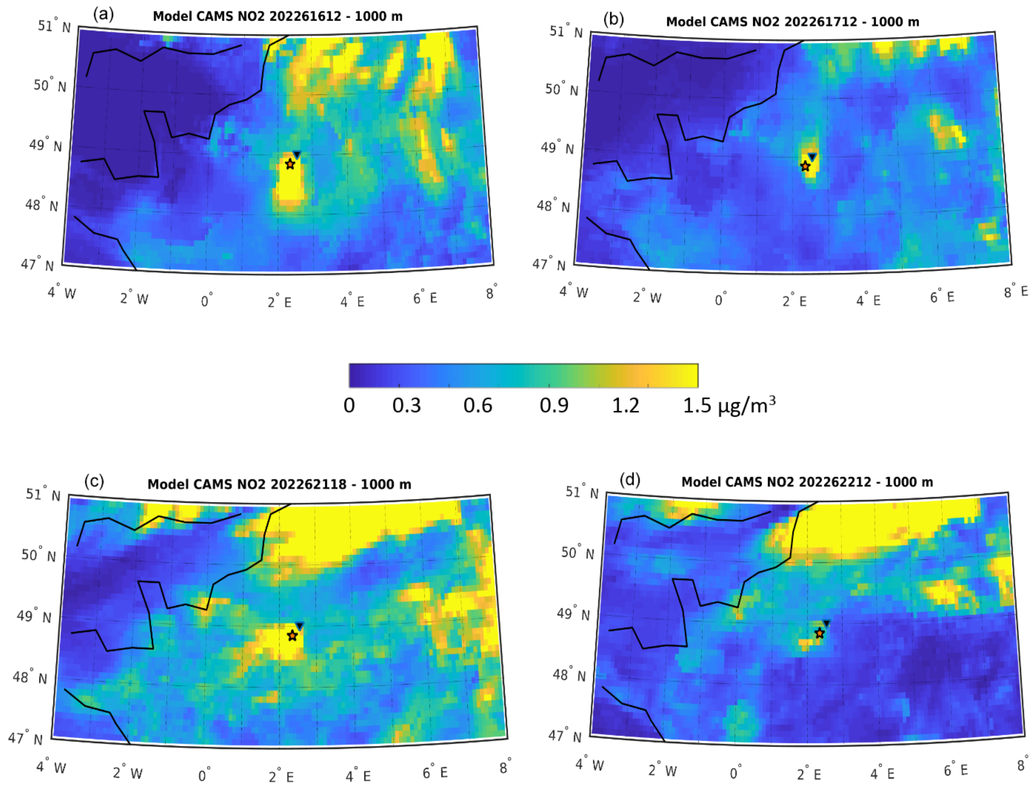

Figure 10. CAMS ensemble mean NO_2 at 1000 m above northern France on 16 and 17 June **(a, b)** when dust plume advection at the PBL top is observed by the aerosol lidar and on 21 and 22 June **(c, d)** when continental aerosol and O_3 plume advection at the PBL top is observed by both lidars. The orange star and dark-blue triangle are respectively the DIAL position and the CDG airport. The color scale is NO_2 concentration in $\mu g\, m^{-3}$.

anticyclonic subsidence in the free troposphere) and O_3 concentrations less than 100 $\mu g\, m^{-3}$ despite the elevated surface temperature in Fig. 2 on 28 June (advection of clean marine air masses).

- On 11–13 July, the horizontal advection shifts back to a northerly flow with transport of O_3-poor air from Benelux (Fig. 4d) on 11 July. This northerly flow is consistent with the Paris plume position in the southwestern part of the Paris region on 12 July (Fig. 4e). On 13 July the flow shifts back to westerly flow, especially above the PBL, bringing back the Paris plume above the city center and leading to high O_3 concentrations.

The position of the Paris O_3 plume seen at 500 m in the CAMS simulations (Figs. 3, 4) corresponds very well to the FLEXPART PES distribution below 1.2 km, showing that the long-range transport analysis on previous days is consistent with the day-to-day variability of the city plume positions. The position of the city's plume on 17 June, which is transported north at 18:00 UT (Fig. 3d), is in fact still to the west of the city at 12:00 UT (not shown) and therefore remains consistent with the distribution of the FLEXPART PES in the city center area at 13:00 UT, which is at a maximum to the north and east of Paris (Fig. S4 top row).

4.3 Comparison of pollution episodes observed during ACROSS

Four pollution periods have been presented in the previous section. All four share conditions conducive to increasing O_3 concentrations in the lower troposphere above Paris: high temperatures (close to or above 30 °C as shown in Fig. 2), formation of an O_3 plume around Paris (see Figs. 3, 4), and storage of O_3 concentrations photochemically produced during the day within a residual nocturnal layer (see Figs. 5, 6). The lowermost tropospheric O_3 columns also show extreme values above 13 DU for these four episodes (see orange rectangles in Fig. 8). However, there are significant differences in the formation of regional-scale pollution plumes or the development of urban boundary layers over Paris to explain the variability of the extremes observed.

- The 14–18 June case study is characterized by a low PBLH < 1.5 km and advection of low O_3 and a dust plume in the free troposphere. Low O_3 concentrations have frequently been observed within dust plumes in western Europe (Bonasoni et al., 2004; Andrey et al., 2014). Nevertheless, the highest O_3 concentrations ($> 170\, \mu g\, m^{-3}$) and lowermost tropospheric columns are found during this episode because European-scale

O_3 photochemical production took place in addition to local photochemistry in the Paris plume. Ozone pollution mitigation due to low O_3 concentrations in the dust plume took place only on 18 June when the PBL and free troposphere mix more effectively.

- For the 21–22 June case study, the PBLH remains below 1.5 km, while there is now advection of a continental plume with elevated O_3 ($> 140\,\mu g\,m^{-3}$) and aerosol concentrations in the free troposphere. The frequent occurrence of clouds in the mid-troposphere and lower surface temperatures than during the first case study explain less O_3 within the Paris plume. The lowermost tropospheric columns are still above 14 DU because advection of the free-tropospheric O_3 layer just above the PBL compensates for lower O_3 production within the PBL.
- For the 28 June case study, although the surface temperature is similar to the second case study, this pollution event is now characterized by elevated PBLH > 2.5 km and no advection of continental plumes above the PBL. Only the Paris plume contributes to the O_3 photochemical production. This is consistent with O_3 concentrations $\leq 110\,\mu g\,m^{-3}$ and lowermost tropospheric columns < 14 DU because O_3 photochemical precursors will be diluted over a greater thickness. Lower cloud cover than during the second case study is not sufficient to compensate for the dilution of O_3 precursor emissions in the PBL.
- The 12–13 July case study, the last pollution event, is also characterized by elevated PBLH > 2.5 km and no advection of a continental plume, even though surface temperatures are as high as during the first pollution event. This is why the lowermost tropospheric columns are again above 14 DU, but contrary to the second case study elevated O_3 concentrations $> 140\,\mu g\,m^{-3}$ are mainly observed within the PBL.

Table 3 summarizes the main characteristics of the summer pollution episodes encountered in Paris. The diversity of long-range transport and its role in O_3 variability mean that this table can be considered sufficiently representative of the conditions that lead to a summer O_3 increase in a city like Paris. Three main conclusions can be drawn from our analysis.

- Westward advection of the pollution plume from continental Europe enhances the O_3 increase over the city of Paris. The contribution of an increase in O_3 background has already been widely demonstrated for other megacities in North America, such as deep stratospheric intrusions or forest fire plumes (see next section). Deep stratospheric intrusions are rare from May to September in northwestern Europe in comparison with North America (Akritidis et al., 2021). Long-range transport of forest fire plumes is also detected in Europe, but at higher altitude (> 5 km) than in North America (Baars et al., 2021), with less of a contribution to the low-troposphere O_3 background. Therefore westward advection of the pollution plume from continental Europe is a significant contribution for the Paris area.
- High temperatures in Paris are often accompanied by a southerly flow carrying Saharan dust in the 2–5 km altitude range over northern France (Israelevich et al., 2012). This study shows that the downward entrainment of the low-O_3 plume at the top of the polluted PBL must be accounted for to understand a possible mitigation of the PBL ozone increase during a summer heat wave.
- The maximum altitudes of the O_3 plume change from 1.5 up to 3 km. The capability of IR satellite observations can be assessed using the ACROSS O_3 profile observations. Our study shows that the IASI 0–3 km tropospheric O_3 column is sensitive to the day-to-day O_3 variability in the lower troposphere, especially when using the AM IASI observations. The significant underestimate of the 0–3 km partial column when the O_3 plume remains below 1.5 km is reduced as soon as the plume maximum altitude exceeds 2 km.

4.4 Comparison with other works

LISTOS 2018–2019 and southwestern USA campaigns took place in places and time periods which can be best compared with ACROSS, i.e., with limited fire and intercontinental pollution and STE. The main difference from LISTOS is the lack of land–sea breeze recirculation for Paris. Ozone concentrations exceeded $200\,\mu g\,m^{-3}$ during LISTOS, with stagnation and land–sea breeze recirculation not seen during ACROSS (Couillard et al., 2021). The regional advection of a European continental O_3 plume and of Saharan dust outbreaks frequently associated with heat wave and pollution episodes is also specific to the Paris area. Regarding the comparison with the TexAQS and TRACER-AQ southeastern USA campaigns, large O_3 concentrations $> 200\,\mu g\,m^{-3}$ are observed near Houston due to the contribution of numerous petrochemical plants in addition to the city emissions (Parrish et al., 2009; Senff et al., 2010), while such O_3 concentrations were never reached during ACROSS. The same conclusion can be drawn from the comparison with the ESCOMPTE campaign O_3 observations when petrochemical plant and ship emission contributions to O_3 plume formation are comparable to the Houston area (Drobinski et al., 2007).

The O_3 long-range transport observed during the southwestern USA campaigns (CABOTS, LVOS) is different from the conditions encountered during ACROSS since STE, fire emission, and Asian pollution plume transport significantly contributed to the O_3 inflow upstream of the local emission sources, especially at altitudes above 2 km (Langford et al., 2022, 2017; Faloona et al., 2020). The latter makes a direct

Table 3. Characteristics of the Paris ozone episodes in summer 2022.

Date (mm/dd)	06/14–18	06/21–22	06/28 (or 07/2)	07/11–13
O_3 plume altitude, km	<1.5	<2.5	<2.5	<3
O_3 plume maximum, $\mu g\,m^{-3}$	170	150	110	150
O_3 0–3 km column, DU	14–16	12–13	12	13–15
High temperature, no clouds	Yes	No	No	Yes
PBL height maximum, km	1.5	1.5	2.5	3.0
PBL O_3 and NO_2 regional increase	Yes	Yes	No	06/13 only
Regional plume above PBL	Dust plume	European pollution	No	No
Bias IASI vs. O_3profiles, DU	−1.5 to −5	0 to −1.5	−2 to −3.5	0 to −2

comparison with the level of O_3 pollution encountered during ACROSS difficult. The main similarity to the ACROSS results is the good agreement between the wide extension of the O_3 streamers shown by both the chemical transport models and the lidar and aircraft observations (Langford et al., 2022; Zhang et al., 2020). Indeed, the CAMS model analysis during ACROSS is consistent with the O_3 observations presented in this paper and also shows that the role of easterly flow from continental Europe replaces that played by the long-range transport of fires and Asian pollution plumes during the southwestern USA campaigns.

5 Conclusions

Four O_3 pollution events with surface concentrations above $100\,\mu g\,m^{-3}$ and lowermost tropospheric columns greater than 14 DU were encountered during the summer 2022 ACROSS campaign. In this work, vertical O_3 profiles measured by a UV DIAL, aircraft (IAGOS), and surface stations at different elevations in the Paris area have been analyzed in synergy with CAMS model simulations at different levels in the lowermost troposphere, with PBL diurnal evolution using a 808 nm microlidar (SLIM), and radiosoundings and with FLEXPART simulations of the regional-scale advection in the Paris PBL. The contribution of DIAL is essential to picture the role of the residual layer O_3 reservoir as well as that of the advection of European continental pollution plumes and Saharan dust plumes above the boundary layer. We have shown in this study that the CAMS simulations of the Paris O_3 plume are consistent with the measurements of the O_3 vertical profiles and that the IASI satellite 0–3 km O_3 partial column day-to-day variability analysis benefits from vertical profile measurements. A satellite 0–3 km partial column with a significant negative bias can be flagged by looking at the maximum altitude level of the lower-tropospheric O_3 plume. In addition to the well-known control of O_3 photochemical production in urban plumes by the surface temperature, by cloud cover, and by the mixing of the surface layer (0–500 m) with the residual layer, this work has shown that the thickness of the PBL during the day and the advection of regional-scale plumes above the PBL can significantly change the O_3 concentrations. With similar cloud cover and air temperature, high O_3 concentrations up to $180\,\mu g\,m^{-3}$ are encountered during the day when PBLH is below 1.5 km, while they remain below $150\,\mu g\,m^{-3}$ when PBLH increases above 2.5 km. Advection of O_3-poor concentrations in the free troposphere during a Saharan dust event is able to mitigate the O_3 photochemical production at the end of the first case study (18 June). On the other hand, the advection of a continental pollution plume with high O_3 concentrations $> 140\,\mu g\,m^{-3}$ maintained high concentrations in the surface layer despite a decrease in temperatures and an increase in cloud cover (22 June). Although the types of regional ozone plumes observed for pollution episodes in Paris are specific to the geographical position of this megacity, the need to take these regional contributions into account in order to understand the variability of pollution episodes in megacities is consistent with what has been observed in past campaigns. Regarding the interaction between urban layer dynamical development and O_3 plume formation during the day, this work is a preliminary study. Further analyses are needed to characterize this interaction in the lowermost troposphere around Paris using additional measurements of wind field and turbulent mixing, e.g., radar and Doppler lidar observations carried out during ACROSS. The microlidar observations will also be improved in the future to continuously monitor both the O_3 profile and the vertical structure of the atmospheric boundary layer. Finally, the O_3 profiles presented in this paper in addition to aircraft chemical observations of the urban plume carried out during the 2022 ACROSS campaign on board the French ATR-42 aircraft will be very valuable datasets to validate future mesoscale simulations of the formation and transport of the O_3 plume around Paris.

Code and data availability. The IASI-FORLI ozone data are available for METOP-B from https://doi.org/10.25326/39 (Hurtmans, 2024a) and for METOP-C from https://doi.org/10.25326/39 (Hurtmans, 2024b).

The AIRPARIF network O_3 data have been downloaded for the Eiffel Tower station from https://data-airparif-asso.opendata.arcgis.

com/datasets/airparif-asso::2022-eiff3/ (AIRPARIF, 2023a) and for the Paris 13 station from https://data-airparif-asso.opendata.arcgis.com/datasets/airparif-asso::2022-pa13/ (AIRPARIF, 2023b).

The QUALAIR station in situ measurements (O_3, temperature) are available on request from camille.viatte@latmos.ipsl.fr.

The IAGOS NetCDF files have been downloaded from https://iagos.aeris-data.fr/download/ (Boulanger et al., 2023).

The NetCDF files with the CAMS ENSEMBLE model hourly analysis of O_3 concentration from 13 June–14 July 2022 for Europe have been downloaded from https://ads.atmosphere.copernicus.eu/datasets/cams-europe-air-quality-reanalyses?tab=download (ECMWF, 2023).

The DIAL data are available on the ACROSS campaign database at https://across.aeris-data.fr/catalogue/?uuid=96d7aa35-40e9-4fc1-baee-a9f7ed2b7b10 (Ancellet, 2023).

The SLIM lidar data are available on request from pascal.genau@latmos.ipsl.fr.

The meteorological radiosounding data are available from https://doi.org/10.25326/448 (Capo, 2023), and the ground-based meteorological data for the Luxembourg and Eiffel Tower stations are available from https://meteo.data.gouv.fr/datasets/6569b51ae64326786e4e8e1a (Meteo France, 2023).

The FLEXPART code version 9.03 was downloaded from https://www.flexpart.eu/roadmap.html (Seibert, 2019) and the meteorological analysis data extraction needed to run the FLEXPART model has been carried out on the ECMWF ATOS data server using the flex_extract version 7.1.3 package downloaded from https://gitlab.phaidra.org/flexpart/flex_extract (Philipp et al., 2023).

Supplement. The supplement related to this article is available online at: https://doi.org/10.5194/acp-24-12963-2024-supplement.

Author contributions. GA and FR designed the work plan and are the PIs of DIAL. CV and CCF provided the infrastructure of the QUALAIR station, and CCF was responsible for the lidar deployment. CV and AB conducted the analysis of the lowermost tropospheric columns and of the IASI data. JP and PG designed the SLIM lidar and conducted the analysis of the PBL structure. PN provided the IAGOS data. JC and AR provided the meteorological soundings and contributed to the analysis and the PBL dynamical development. GA processed the DIAL data and conducted the overall data synthesis. All contributed to the paper preparation.

Competing interests. The contact author has declared that none of the authors has any competing interests.

Special issue statement. This article is part of the special issue "Atmospheric Chemistry of the Suburban Forest – multiplatform observational campaign of the chemistry and physics of mixed urban and biogenic emissions". It is not associated with a conference.

Acknowledgements. IASI is a joint mission of EUMETSAT and the Centre National d'Etudes Spatiales (CNES, France). ULB-LATMOS is acknowledged for the development of the FORLI retrieval algorithm, and the AC SAF project of EUMETSAT is acknowledged for providing IASI O_3 data.

The authors would like to acknowledge the QUALAIR team and infrastructure for their scientific support.

The authors acknowledge the AERIS data infrastructure for providing access to the IASI-FORLI data and for hosting the IAGOS and ACROSS database. The AIRPARIF air quality agency is gratefully acknowledged for providing the O_3 surface data for the Paris 13 and Eiffel Tower stations. The European Centre for Medium-Range Weather Forecasts (ECMWF) is acknowledged for the provision of meteorological analysis data, and the FLEXPART development team is acknowledged for the provision of the FLEXPART 9.2 model version used in this publication.

Christopher Cantrell, the PI of the ACROSS campaign, is also gratefully acknowledged for his support. For the radiosoundings and standard weather observations this project benefited from access to the National Instrument Moyens Mobiles, which is part of the research infrastructure ACTRIS-FR.

Financial support. This research has been supported by the Centre National de la Recherche Scientifique (LEFE-CHAT, ACROSS project), the Agence Nationale de la Recherche (grant no. ANR-20-CE22-0013), and the Sorbonne Université (UFR, TEB, Fonctionnement Plateforme QUALAIR). Météo-France and the WMO supported the meteorological observations as part of the Research Demonstration Project for the Paris Olympics 2024 coordinated by Valery Masson.

Review statement. This paper was edited by Jeffrey Geddes and reviewed by two anonymous referees.

References

Akritidis, D., Pozzer, A., Flemming, J., Inness, A., and Zanis, P.: A Global Climatology of Tropopause Folds in CAMS and MERRA-2 Reanalyses, J. Geophys. Res.-Atmos., 126, e2020JD034115, https://doi.org/10.1029/2020JD034115, 2021.

AIRPARIF: Ozone concentrations of station Tour Eiffel 3ème étage for year 2022, AIRPARIF [data set], https://data-airparif-asso.opendata.arcgis.com/datasets/airparif-asso::2022-eiff3/ (last access: 25 September 2023), 2023a.

AIRPARIF: Ozone concentrations of station Paris 13 for year 2022, AIRPARIF [data set], https://data-airparif-asso.opendata.arcgis.com/datasets/airparif-asso::2022-pa13/ (25 September 2023), 2023b.

Ancellet, G.: ACROSS_LATMOS_SU-QUALAIR_O3-profile-Lidar, AERIS [data set], https://across.aeris-data.fr/catalogue/

?uuid=96d7aa35-40e9-4fc1-baee-a9f7ed2b7b10 (last access: 4 July 2023), 2023.

Ancellet, G. and Ravetta, F.: Compact airborne lidar for tropospheric ozone: description and field measurements, Appl. Opt., 37, 5509–5521, https://doi.org/10.1364/AO.37.005509, 1998.

Ancellet, G. and Ravetta, F.: Analysis and validation of ozone variability observed by lidar during the ESCOMPTE-2001 campaign, Atmos. Res., 74, 435–459, https://doi.org/10.1016/j.atmosres.2004.10.003, 2005.

Andrey, J., Cuevas, E., Parrondo, M., Alonso-Pérez, S., Redondas, A., and Gil-Ojeda, M.: Quantification of ozone reductions within the Saharan air layer through a 13-year climatologic analysis of ozone profiles, Atmos. Environ., 84, 28–34, https://doi.org/10.1016/j.atmosenv.2013.11.030, 2014.

Antón, M., Loyola, D., Clerbaux, C., López, M., Vilaplana, J., Bañón, M., Hadji-Lazaro, J., Valks, P., Hao, N., Zimmer, W., Coheur, P., Hurtmans, D., and Alados-Arboledas, L.: Validation of the MetOp-A total ozone data from GOME-2 and IASI using reference ground-based measurements at the Iberian Peninsula, Remote Sens. Environ., 115, 1380–1386, https://doi.org/10.1016/j.rse.2011.01.018, 2011.

Baars, H., Radenz, M., Floutsi, A. A., Engelmann, R., Althausen, D., Heese, B., Ansmann, A., Flament, T., Dabas, A., Trapon, D., Reitebuch, O., Bley, S., and Wandinger, U.: Californian Wildfire Smoke Over Europe: A First Example of the Aerosol Observing Capabilities of Aeolus Compared to Ground-Based Lidar, Geophys. Res. Lett., 48, e2020GL092194, https://doi.org/10.1029/2020GL092194, 2021.

Bonasoni, P., Cristofanelli, P., Calzolari, F., Bonafè, U., Evangelisti, F., Stohl, A., Zauli Sajani, S., van Dingenen, R., Colombo, T., and Balkanski, Y.: Aerosol-ozone correlations during dust transport episodes, Atmos. Chem. Phys., 4, 1201–1215, https://doi.org/10.5194/acp-4-1201-2004, 2004.

Boulanger, D., Blot, M., Cousin, J. M., and Cleris, S.: IAGOS Level 2 ozone mixing ratio, IAGOS [dataset], https://iagos.aeris-data.fr/download/ (19 November 2023), 2023.

Boynard, A., Clerbaux, C., Coheur, P.-F., Hurtmans, D., Turquety, S., George, M., Hadji-Lazaro, J., Keim, C., and Meyer-Arnek, J.: Measurements of total and tropospheric ozone from IASI: comparison with correlative satellite, ground-based and ozonesonde observations, Atmos. Chem. Phys., 9, 6255–6271, https://doi.org/10.5194/acp-9-6255-2009, 2009.

Boynard, A., Hurtmans, D., Koukouli, M. E., Goutail, F., Bureau, J., Safieddine, S., Lerot, C., Hadji-Lazaro, J., Wespes, C., Pommereau, J.-P., Pazmino, A., Zyrichidou, I., Balis, D., Barbe, A., Mikhailenko, S. N., Loyola, D., Valks, P., Van Roozendael, M., Coheur, P.-F., and Clerbaux, C.: Seven years of IASI ozone retrievals from FORLI: validation with independent total column and vertical profile measurements, Atmos. Meas. Tech., 9, 4327–4353, https://doi.org/10.5194/amt-9-4327-2016, 2016.

Boynard, A., Hurtmans, D., Garane, K., Goutail, F., Hadji-Lazaro, J., Koukouli, M. E., Wespes, C., Vigouroux, C., Keppens, A., Pommereau, J.-P., Pazmino, A., Balis, D., Loyola, D., Valks, P., Sussmann, R., Smale, D., Coheur, P.-F., and Clerbaux, C.: Validation of the IASI FORLI/EUMETSAT ozone products using satellite (GOME-2), ground-based (Brewer–Dobson, SAOZ, FTIR) and ozonesonde measurements, Atmos. Meas. Tech., 11, 5125–5152, https://doi.org/10.5194/amt-11-5125-2018, 2018.

Capo, J.: PANAME 2022 meteorological radiosoundings version 2, [data set], https://doi.org/10.25326/448, 2023.

Caputi, D. J., Faloona, I., Trousdell, J., Smoot, J., Falk, N., and Conley, S.: Residual layer ozone, mixing, and the nocturnal jet in California's San Joaquin Valley, Atmos. Chem. Phys., 19, 4721–4740, https://doi.org/10.5194/acp-19-4721-2019, 2019.

Couillard, M. H., Schwab, M. J., Schwab, J. J., Lu, C.-H. S., Joseph, E., Stutsrim, B., Shrestha, B., Zhang, J., Knepp, T. N., and Gronoff, G. P.: Vertical Profiles of Ozone Concentrations in the Lower Troposphere Downwind of New York City During LISTOS 2018–2019, J. Geophys. Res.-Atmos., 126, e2021JD035108, https://doi.org/10.1029/2021JD035108, 2021.

Daum, P. H., Kleinman, L. I., Springston, S. R., Nunnermacker, L. J., Lee, Y.-N., Weinstein-Lloyd, J., Zheng, J., and Berkowitz, C. M.: Origin and properties of plumes of high ozone observed during the Texas 2000 Air Quality Study (TexAQS 2000), J. Geophys. Res.-Atmos., 109, D17306, https://doi.org/10.1029/2003JD004311, 2004.

Drobinski, P., Saïd, F., Ancellet, G., Arteta, J., Augustin, P., Bastin, S., Brut, A., Caccia, J., Campistron, B., Cautenet, S., Colette, A., Coll, I., Corsmeier, U., Cros, B., Dabas, A., Delbarre, H., Dufour, A., Durand, P., Guénard, V., Hasel, M., Kalthoff, N., C.Kottmeier, Lasry, F., Lemonsu, A., Lohou, F., Masson, V., Menut, L., Moppert, C., Peuch, V., Puygrenier, V., Reitebuch, O., and Vautard, R.: Regional transport and dilution during high-pollution episodes in southern France: Summary of findings from the Field Experiment to Constraint Models of Atmospheric Pollution and Emissions Transport (ESCOMPTE), J. Geophys. Res., 112, D13105, https://doi.org/10.1029/2006JD007494, 2007.

Dufour, G., Eremenko, M., Orphal, J., and Flaud, J.-M.: IASI observations of seasonal and day-to-day variations of tropospheric ozone over three highly populated areas of China: Beijing, Shanghai, and Hong Kong, Atmos. Chem. Phys., 10, 3787–3801, https://doi.org/10.5194/acp-10-3787-2010, 2010.

Dupont, E., Pelon, J., and Flamant, C.: Study of the moist Convective Boundary Layer structure by backscattering lidar, Bound.-Lay. Meteorol., 69, 1–25, https://doi.org/10.1007/BF00713292, 1994.

ECMWF: CAMS European air quality reanalyses, [data set], https://ads.atmosphere.copernicus.eu/datasets/cams-europe-air-quality-reanalyses?tab=download (last access: 8 November 2023), 2023.

Eremenko, M., Dufour, G., Foret, G., Keim, C., Orphal, J., Beekmann, M., Bergametti, G., and Flaud, J.-M.: Tropospheric ozone distributions over Europe during the heat wave in July 2007 observed from infrared nadir spectra recorded by IASI, Geophys. Res. Lett., 35, L18805, https://doi.org/10.1029/2008GL034803, 2008.

Faloona, I. C., Chiao, S., Eiserloh, A. J., Alvarez, R. J., Kirgis, G., Langford, A. O., Senff, C. J., Caputi, D., Hu, A., Iraci, L. T., Yates, E. L., Marrero, J. E., Ryoo, J.-M., Conley, S., Tanrikulu, S., Xu, J., and Kuwayama, T.: The California Baseline Ozone Transport Study (CABOTS), B. Am. Meteorol. Soc., 101, E427–E445, https://doi.org/10.1175/BAMS-D-18-0302.1, 2020.

Flamant, C. and Pelon, J.: Atmospheric boundary-layer structure over the Mediterranean during a Tramontane event, Q. J. Roy. Meteor. Soc., 122, 1741–1778, https://doi.org/10.1002/qj.49712253602, 1996.

Fowler, D., Amann, M., Anderson, R., Ashmore, M., Cox, P., Depledge, M., Derwent, D., Grennfelt, P., Hewitt, N., Hov, O., Jenkin, M., Kelly, F., Liss, P., Pilling, M., Pyle, J., Slingo, J., and Stevenson, D.: Ground-level ozone in the 21st century: Future trends, impacts and policy implications, Vol. 15 of Royal Society Science Policy Report, 8th edn., ISBN 978-0-85403-713-1, The Royal Society Science Policy, London, 2008.

Güsten, H., Heinrich, G., and Sprung, D.: Nocturnal depletion of ozone in the Upper Rhine Valley, Atmos. Environ., 32, 1195–1202, https://doi.org/10.1016/S1352-2310(97)00195-7, 1998.

Hurtmans, D., Coheur, P.-F., Wespes, C., Clarisse, L., Scharf, O., Clerbaux, C., Hadji-Lazaro, J., George, M., and Turquety, S.: FORLI radiative transfer and retrieval code for IASI, J. Quant. Spectrosc. Ra., 113, 1391–1408, https://doi.org/10.1016/j.jqsrt.2012.02.036, 2012.

Hurtmans, D.: Daily IASI/Metop-B ULB-LATMOS ozone (O_3) L2 product, AERIS [data set], https://doi.org/10.25326/39, 2024a

Hurtmans, D.: Daily IASI/Metop-B ULB-LATMOS ozone (O_3) L2 product, AERIS [data set], https://doi.org/10.25326/39, 2024b

Inness, A., Ades, M., Agustí-Panareda, A., Barré, J., Benedictow, A., Blechschmidt, A.-M., Dominguez, J. J., Engelen, R., Eskes, H., Flemming, J., Huijnen, V., Jones, L., Kipling, Z., Massart, S., Parrington, M., Peuch, V.-H., Razinger, M., Remy, S., Schulz, M., and Suttie, M.: The CAMS reanalysis of atmospheric composition, Atmos. Chem. Phys., 19, 3515–3556, https://doi.org/10.5194/acp-19-3515-2019, 2019.

Israelevich, P., Ganor, E., Alpert, P., Kishcha, P., and Stupp, A.: Predominant transport paths of Saharan dust over the Mediterranean Sea to Europe, J. Geophys. Res.-Atmos., 117, D02205, https://doi.org/10.1029/2011JD016482, 2012.

Keppens, A., Lambert, J.-C., Granville, J., Hubert, D., Verhoelst, T., Compernolle, S., Latter, B., Kerridge, B., Siddans, R., Boynard, A., Hadji-Lazaro, J., Clerbaux, C., Wespes, C., Hurtmans, D. R., Coheur, P.-F., van Peet, J. C. A., van der A, R. J., Garane, K., Koukouli, M. E., Balis, D. S., Delcloo, A., Kivi, R., Stübi, R., Godin-Beekmann, S., Van Roozendael, M., and Zehner, C.: Quality assessment of the Ozone_cci Climate Research Data Package (release 2017) – Part 2: Ground-based validation of nadir ozone profile data products, Atmos. Meas. Tech., 11, 3769–3800, https://doi.org/10.5194/amt-11-3769-2018, 2018.

Klein, A., Ancellet, G., Ravetta, F., Thomas, J. L., and Pazmino, A.: Characterizing the seasonal cycle and vertical structure of ozone in Paris, France using four years of ground based LIDAR measurements in the lowermost troposphere, Atmos. Environ., 167, 603–615, https://doi.org/10.1016/j.atmosenv.2017.08.016, 2017.

Klein, A., Ravetta, F., Thomas, J. L., Ancellet, G., Augustin, P., Wilson, R., Dieudonné, E., Fourmentin, M., Delbarre, H., and Pelon, J.: Influence of vertical mixing and nighttime transport on surface ozone variability in the morning in Paris and the surrounding region, Atmos. Environ., 197, 92–102, https://doi.org/10.1016/j.atmosenv.2018.10.009, 2019.

Klett, J. D.: Lidar inversion with variable backscatter/extinction ratios, Appl. Opt., 24, 1638–1643, https://doi.org/10.1364/AO.24.001638, 1985.

Langford, A. O., Alvarez II, R. J., Brioude, J., Fine, R., Gustin, M. S., Lin, M. Y., Marchbanks, R. D., Pierce, R. B., Sandberg, S. P., Senff, C. J., Weickmann, A. M., and Williams, E. J.: Entrainment of stratospheric air and Asian pollution by the convective boundary layer in the southwestern U.S., J. Geophys. Res.-Atmos., 122, 1312–1337, https://doi.org/10.1002/2016JD025987, 2017.

Langford, A. O., Alvarez II, R. J., Kirgis, G., Senff, C. J., Caputi, D., Conley, S. A., Faloona, I. C., Iraci, L. T., Marrero, J. E., McNamara, M. E., Ryoo, J.-M., and Yates, E. L.: Intercomparison of lidar, aircraft, and surface ozone measurements in the San Joaquin Valley during the California Baseline Ozone Transport Study (CABOTS), Atmos. Meas. Tech., 12, 1889–1904, https://doi.org/10.5194/amt-12-1889-2019, 2019.

Langford, A. O., Senff, C. J., Alvarez II, R. J., Aikin, K. C., Baidar, S., Bonin, T. A., Brewer, W. A., Brioude, J., Brown, S. S., Burley, J. D., Caputi, D. J., Conley, S. A., Cullis, P. D., Decker, Z. C. J., Evan, S., Kirgis, G., Lin, M., Pagowski, M., Peischl, J., Petropavlovskikh, I., Pierce, R. B., Ryerson, T. B., Sandberg, S. P., Sterling, C. W., Weickmann, A. M., and Zhang, L.: The *Fires, Asian, and Stratospheric Transport*–Las Vegas Ozone Study (*FAST*-LVOS), Atmos. Chem. Phys., 22, 1707–1737, https://doi.org/10.5194/acp-22-1707-2022, 2022.

Lin, M., Fiore, A. M., Horowitz, L. W., Cooper, O. R., Naik, V., Holloway, J., Johnson, B. J., Middlebrook, A. M., Oltmans, S. J., Pollack, I. B., Ryerson, T. B., Warner, J. X., Wiedinmyer, C., Wilson, J., and Wyman, B.: Transport of Asian ozone pollution into surface air over the western United States in spring, J. Geophys. Res.-Atmos., 117, D00V07, https://doi.org/10.1029/2011JD016961, 2012.

Liu, X., Wang, Y., Wasti, S., Li, W., Soleimanian, E., Flynn, J., Griggs, T., Alvarez, S., Sullivan, J. T., Roots, M., Twigg, L., Gronoff, G., Berkoff, T., Walter, P., Estes, M., Hair, J. W., Shingler, T., Scarino, A. J., Fenn, M., and Judd, L.: Evaluating WRF-GC v2.0 predictions of boundary layer height and vertical ozone profile during the 2021 TRACER-AQ campaign in Houston, Texas, Geosci. Model Dev., 16, 5493–5514, https://doi.org/10.5194/gmd-16-5493-2023, 2023.

Ma, S., Tong, D., Lamsal, L., Wang, J., Zhang, X., Tang, Y., Saylor, R., Chai, T., Lee, P., Campbell, P., Baker, B., Kondragunta, S., Judd, L., Berkoff, T. A., Janz, S. J., and Stajner, I.: Improving predictability of high-ozone episodes through dynamic boundary conditions, emission refresh and chemical data assimilation during the Long Island Sound Tropospheric Ozone Study (LISTOS) field campaign, Atmos. Chem. Phys., 21, 16531–16553, https://doi.org/10.5194/acp-21-16531-2021, 2021.

Marécal, V., Peuch, V.-H., Andersson, C., Andersson, S., Arteta, J., Beekmann, M., Benedictow, A., Bergström, R., Bessagnet, B., Cansado, A., Chéroux, F., Colette, A., Coman, A., Curier, R. L., Denier van der Gon, H. A. C., Drouin, A., Elbern, H., Emili, E., Engelen, R. J., Eskes, H. J., Foret, G., Friese, E., Gauss, M., Giannaros, C., Guth, J., Joly, M., Jaumouillé, E., Josse, B., Kadygrov, N., Kaiser, J. W., Krajsek, K., Kuenen, J., Kumar, U., Liora, N., Lopez, E., Malherbe, L., Martinez, I., Melas, D., Meleux, F., Menut, L., Moinat, P., Morales, T., Parmentier, J., Piacentini, A., Plu, M., Poupkou, A., Queguiner, S., Robertson, L., Rouïl, L., Schaap, M., Segers, A., Sofiev, M., Tarasson, L., Thomas, M., Timmermans, R., Valdebenito, Á., van Velthoven, P., van Versendaal, R., Vira, J., and Ung, A.: A regional air quality forecasting system over Europe: the MACC-II daily ensemble production, Geosci. Model Dev., 8, 2777–2813, https://doi.org/10.5194/gmd-8-2777-2015, 2015.

Mariage, V., Pelon, J., Blouzon, F., Victori, S., Geyskens, N., Amarouche, N., Drezen, C., Guillot, A., Calzas, M., Garracio, M., Wegmuller, N., Sennéchael, N., and Provost, C.: IAOOS microlidar-on-buoy development and first atmospheric observations obtained during 2014 and 2015 arctic drifts, Opt. Express, 25, A73–A84, https://doi.org/10.1364/OE.25.000A73, 2017.

Menut, L., Flamant, C., Pelon, J., and Flamant, P. H.: Urban boundary-layer height determination from lidar measurements over the Paris area, Appl. Opt., 38, 945–954, https://doi.org/10.1364/AO.38.000945, 1999.

Meteo France: Operational in-situ meteorological data, Meteo France [data set], https://meteo.data.gouv.fr/datasets/6569b51ae64326786e4e8e1a (last access: 25 September 2023), 2023.

Monks, P. S., Archibald, A. T., Colette, A., Cooper, O., Coyle, M., Derwent, R., Fowler, D., Granier, C., Law, K. S., Mills, G. E., Stevenson, D. S., Tarasova, O., Thouret, V., von Schneidemesser, E., Sommariva, R., Wild, O., and Williams, M. L.: Tropospheric ozone and its precursors from the urban to the global scale from air quality to short-lived climate forcer, Atmos. Chem. Phys., 15, 8889–8973, https://doi.org/10.5194/acp-15-8889-2015, 2015.

Nédélec, P., Blot, R., Boulanger, D., Athier, G., Cousin, J.-M., Gautron, B., Petzold, A., Volz-Thomas, A., and Thouret, V.: Instrumentation on commercial aircraft for monitoring the atmospheric composition on a global scale: the IAGOS system, technical overview of ozone and carbon monoxide measurements, Tellus B, 67, 27791, https://doi.org/10.3402/tellusb.v67.27791, 2015.

Neu, U., Künzle, T., and Wanner, H.: On the relation between ozone storage in the residual layer and daily variation in near-surface ozone concentration – A case study, Bound.-Lay. Meteorol., 69, 221–247, https://doi.org/10.1007/BF00708857, 1994.

O'Connor, E. J., Illingworth, A. J., and Hogan, R. J.: A Technique for Autocalibration of Cloud Lidar, J. Atmos. Ocean. Tech., 21, 777–786, https://doi.org/10.1175/1520-0426(2004)021<0777:ATFAOC>2.0.CO;2, 2004.

Parrish, D. D., Allen, D. T., Bates, T. S., Estes, M., Fehsenfeld, F. C., Feingold, G., Ferrare, R., Hardesty, R. M., Meagher, J. F., Nielsen-Gammon, J. W., Pierce, R. B., Ryerson, T. B., Seinfeld, J. H., and Williams, E. J.: Overview of the Second Texas Air Quality Study (TexAQS II) and the Gulf of Mexico Atmospheric Composition and Climate Study (GoMACCS), J. Geophys. Res.-Atmos., 114, D00F13, https://doi.org/10.1029/2009JD011842, 2009.

Pelon, J., Mallet, M., Mariscal, A., Goloub, P., Tanré, D., Bou Karam, D., Flamant, C., Haywood, J., Pospichal, B., and Victori, S.: Microlidar observations of biomass burning aerosol over Djougou (Benin) during African Monsoon Multidisciplinary Analysis Special Observation Period 0: Dust and Biomass-Burning Experiment, J. Geophys. Res.-Atmos., 113, D00C18, https://doi.org/10.1029/2008JD009976, 2008.

Philipp, A., Haimberger, L., and Seibert, P.: Preprocessing model of ECMWF input data (flex_extract version 7.1.3), GitLab [code], https://gitlab.phaidra.org/flexpart/flex_extract (last access: 22 March 2023), 2023.

Pommier, M., Clerbaux, C., Law, K. S., Ancellet, G., Bernath, P., Coheur, P.-F., Hadji-Lazaro, J., Hurtmans, D., Nédélec, P., Paris, J.-D., Ravetta, F., Ryerson, T. B., Schlager, H., and Weinheimer, A. J.: Analysis of IASI tropospheric O_3 data over the Arctic during POLARCAT campaigns in 2008, Atmos. Chem. Phys., 12, 7371–7389, https://doi.org/10.5194/acp-12-7371-2012, 2012.

Rodgers, C. D.: Inverse Methods for Atmospheric Sounding, WORLD SCIENTIFIC, https://doi.org/10.1142/3171, 2000.

Rodgers, C. D. and Connor, B. J.: Intercomparison of remote sounding instruments, J. Geophys. Res.-Atmos., 108, 4116, https://doi.org/10.1029/2002JD002299, 2003.

Ryerson, T. B., Andrews, A. E., Angevine, W. M., Bates, T. S., Brock, C. A., Cairns, B., Cohen, R. C., Cooper, O. R., de Gouw, J. A., Fehsenfeld, F. C., Ferrare, R. A., Fischer, M. L., Flagan, R. C., Goldstein, A. H., Hair, J. W., Hardesty, R. M., Hostetler, C. A., Jimenez, J. L., Langford, A. O., McCauley, E., McKeen, S. A., Molina, L. T., Nenes, A., Oltmans, S. J., Parrish, D. D., Pederson, J. R., Pierce, R. B., Prather, K., Quinn, P. K., Seinfeld, J. H., Senff, C. J., Sorooshian, A., Stutz, J., Surratt, J. D., Trainer, M., Volkamer, R., Williams, E. J., and Wofsy, S. C.: The 2010 California Research at the Nexus of Air Quality and Climate Change (CalNex) field study, J. Geophys. Res.-Atmos., 118, 5830–5866, https://doi.org/10.1002/jgrd.50331, 2013.

Safieddine, S., Clerbaux, C., George, M., Hadji-Lazaro, J., Hurtmans, D., Coheur, P.-F., Wespes, C., Loyola, D., Valks, P., and Hao, N.: Tropospheric ozone and nitrogen dioxide measurements in urban and rural regions as seen by IASI and GOME-2, J. Geophys. Res.-Atmos., 118, 10555–10566, https://doi.org/10.1002/jgrd.50669, 2013.

Sarrat, C., Lemonsu, A., Masson, V., and Guedalia, D.: Impact of urban heat island on regional atmospheric pollution, Atmos. Environ., 40, 1743–1758, https://doi.org/10.1016/j.atmosenv.2005.11.037, 2006.

Seibert, P.: FLEXible PARTicle dispersion model (FLEXPART) version 9.03, Flexpart [code], https://www.flexpart.eu/roadmap.html (last access: 7 January 2019), 2024.

Seinfeld, J. and Pandis, S.: Atmospheric Chemistry and Physics: From Air Pollution to Climate Change, Wiley, ISBN 9781118947401, 2016.

Senff, C. J., Alvarez II, R. J., Hardesty, R. M., Banta, R. M., and Langford, A. O.: Airborne lidar measurements of ozone flux downwind of Houston and Dallas, J. Geophys. Res.-Atmos., 115, D20307, https://doi.org/10.1029/2009JD013689, 2010.

Stohl, A. and Seibert, P.: Accuracy of trajectories as determined from the conservation of meteorological tracers, Q. J. Roy. Meteor. Soc., 124, 1465–1484, https://doi.org/10.1002/qj.49712454907, 1998.

Stohl, A., Eckhardt, S., Forster, C., James, P., Spichtinger, N., and Seibert, P.: A replacement for simple back trajectory calculations in the interpretation of atmospheric trace substance measurements, Atmos. Environ., 36, 4635–4648, https://doi.org/10.1016/S1352-2310(02)00416-8, 2002.

Stull, R.: An Introduction to Boundary Layer Meteorology, Atmospheric and Oceanographic Sciences Library, Springer Netherlands, ISBN 9789027727695, https://doi.org/10.1007/978-94-009-3027-8, 1988.

Sullivan, J. T., Rabenhorst, S. D., Dreessen, J., McGee, T. J., Delgado, R., Twigg, L., and Sumnicht, G.: Lidar observations revealing transport of O_3 in the presence of a nocturnal low-level jet: Regional implications for "next-day" pollution, Atmos. Environ., 158, 160–171, https://doi.org/10.1016/j.atmosenv.2017.03.039, 2017.

Thouret, V., Marenco, A., Logan, J. A., Nédélec, P., and Grouhel, C.: Comparisons of ozone measurements from the MOZAIC airborne program and the ozone sounding network at eight locations, J. Geophys. Res.-Atmos., 103, 25695–25720, https://doi.org/10.1029/98JD02243, 1998.

Vautard, R., Menut, L., Beekmann, M., Chazette, P., Flamant, P. H., Gombert, D., Guédalia, D., Kley, D., Lefebvre, M.-P., Martin, D., Mégie, G., Perros, P., and Toupance, G.: A synthesis of the Air Pollution Over the Paris Region (ESQUIF) field campaign, J. Geophys. Res.-Atmos., 108, 8558, https://doi.org/10.1029/2003JD003380, 2003.

Viatte, C., Gaubert, B., Eremenko, M., Hase, F., Schneider, M., Blumenstock, T., Ray, M., Chelin, P., Flaud, J.-M., and Orphal, J.: Tropospheric and total ozone columns over Paris (France) measured using medium-resolution ground-based solar-absorption Fourier-transform infrared spectroscopy, Atmos. Meas. Tech., 4, 2323–2331, https://doi.org/10.5194/amt-4-2323-2011, 2011.

Wagner, A., Bennouna, Y., Blechschmidt, A.-M., Brasseur, G., Chabrillat, S., Christophe, Y., Errera, Q., Eskes, H., Flemming, J., Hansen, K. M., Inness, A., Kapsomenakis, J., Langerock, B., Richter, A., Sudarchikova, N., Thouret, V., and Zerefos, C.: Comprehensive evaluation of the Copernicus Atmosphere Monitoring Service (CAMS) reanalysis against independent observations: Reactive gases, Elem. Sci. Anth., 9, 00171, https://doi.org/10.1525/elementa.2020.00171, 2021.

Wang, B., Kuang, S., Pfister, G. G., Pour-Biazar, A., Buchholz, R. R., Langford, A. O., and Newchurch, M. J.: Impact of the 2016 Southeastern US Wildfires on the Vertical Distribution of Ozone and Aerosol at Huntsville, Alabama, J. Geophys. Res.-Atmos., 126, e2021JD034796, https://doi.org/10.1029/2021JD034796, 2021.

Wespes, C., Hurtmans, D., Clerbaux, C., Boynard, A., and Coheur, P.-F.: Decrease in tropospheric O_3 levels in the Northern Hemisphere observed by IASI, Atmos. Chem. Phys., 18, 6867–6885, https://doi.org/10.5194/acp-18-6867-2018, 2018.

Zaveri, R. A., Berkowitz, C. M., Kleinman, L. I., Springston, S. R., Doskey, P. V., Lonneman, W. A., and Spicer, C. W.: Ozone production efficiency and NOx depletion in an urban plume: Interpretation of field observations and implications for evaluating O_3-NO_x-VOC sensitivity, J. Geophys. Res.-Atmos., 108, 4436, https://doi.org/10.1029/2002JD003144, 2003.

Zhang, L., Lin, M., Langford, A. O., Horowitz, L. W., Senff, C. J., Klovenski, E., Wang, Y., Alvarez II, R. J., Petropavlovskikh, I., Cullis, P., Sterling, C. W., Peischl, J., Ryerson, T. B., Brown, S. S., Decker, Z. C. J., Kirgis, G., and Conley, S.: Characterizing sources of high surface ozone events in the southwestern US with intensive field measurements and two global models, Atmos. Chem. Phys., 20, 10379–10400, https://doi.org/10.5194/acp-20-10379-2020, 2020.